

A proposal to the Jefferson Lab Program Advisory
Committee (PAC35)

**Precision Measurement of the
Neutron Magnetic Form Factor
at $Q^2=16.0$ and 18.0 (GeV/c)² by the Ratio
Method**

F. Benmokhtar, G.B. Franklin, B. Quinn (spokesperson), R. Schumacher
Carnegie Mellon University, Pittsburgh, PA 15213

A. Camsonne, J.P. Chen, E. Chudakov, C. DeJager,
P. Degtyarenko, J. Gomez, O. Hansen, D. W. Higinbotham,
M. Jones, J. LeRose, R. Michaels, S. Nanda, A. Saha, B. Sawatzky
B. Wojtsekhowski (spokesperson and contact person)
Thomas Jefferson National Accelerator Facility, Newport News, VA 23606

L. El Fassi, R. Gilman (spokesperson), G. Kumbartzki, R. Ransome, E. Schulte
Rutgers University, Piscataway, NJ 08854

T. Averett, C.F. Perdrisat
College of William and Mary

D. Castelluccio, E. Cisbani, F. Garibaldi, S. Frullani
INFN-Rome Sanita Group and Istituto Superiore di Sanita, Rome, Italy

F. Meddi and G. Urciuoli
INFN-Rome and University "La Sapienza", Rome, Italy

M. Capogni
INFN-Rome Sanita Group and ENEA Casaccia, Rome, Italy

H. Baghdasaryan, G. Cates, D. Day, N. Kalantarians, R. Lindgren, N. Liyanage,
V. Nelyubin, B. E. Norum, K. D. Paschke, S. Riordan, X. Zheng
University of Virginia, Charlottesville, VA 22901

W. Brooks
Universidad Tecnica Federico Santa Maria, Valparaiso, Chile

V. Punjabi, M. Khandaker W. Boeglin, P. Markowitz, J. Reinhold
Norfolk State University *Florida International University, Fl*

J. Annand, D. Hamilton, D. Ireland, R. Kaiser, K. Livingston,
I. MacGregor, B. Seitz, and G. Rosner
University of Glasgow, Glasgow, Scotland

D. Nikolenko, I. Rachek, Yu. Shestakov
Budker Institute, Novosibirsk, Russia

R. De Leo, L. La Gamba, S. Marrone, E. Nappi
INFN, Bari, Italy

M. Mihovilovič, S. Širca
Jožef Stefan Institute and Dept. of Physics, University of Ljubljana, Slovenia

J. Gilfoyle
University of Richmond, Richmond, VA

J. Lichtenstadt, I. Pomerantz, E. Piassetzky, G. Ron
Tel Aviv University, Israel

A. Glamazdin
Kharkov Institute of Physics and Technology, Kharkov 310077, Ukraine

J. Calarco, K. Slifer
University of New Hampshire, Durham, NH 03824

B. Vlahovic
North Carolina Central University, Durham, NC 03824

A. Sarty
Saint Mary's University, Nova Scotia, Canada B3H 3C3

K. Aniol and D. J. Magaziotis
Cal State University, Los Angeles, CA 90032

S. Abrahamyan, S. Mayilyan, A. Shahinyan, H. Voskanyan
Yerevan Physics Institute, Yerevan, Armenia

D. Glazier and D. Watts
University of Edinburgh, Edinburgh, Scotland

B. Bertozzi, S. Gilad, V. Sulkosky
Massachusetts Institute of Technology, Cambridge, MA 02139

and
The Hall A Collaboration

December 14, 2009

Abstract

We propose to make high-precision measurement of the neutron's magnetic form factor, G_M^n , at $Q^2 = 16.0$ and 18.0 $(\text{GeV}/c)^2$. This would extend the coverage beyond the seven kinematic points already approved in experiment E-09-019. A major improvement of experimental equipment from that originally planned in E-09-019 will permit the use of much higher luminosity for these high- Q^2 points while reducing background rates and simplifying the experiment installation and analysis. The proposed experiment would run contiguously with E-09-019 to take advantage of calibrations and systematics studies made possible by the copious statistics available at lower Q^2 . The new data will push the Q^2 range for G_M^n measurements beyond any other existing or planned experiments.

In the proposed experiment, systematic errors are greatly reduced by the use of the “ratio” method in which G_M^n is extracted from the ratio of neutron-coincident to proton-coincident quasi-elastic electron scattering from the deuteron. The experiment would be performed in Hall A using the BigBite spectrometer to detect the scattered electrons and the HCal to detect both neutrons and protons. A large aperture dipole magnet on the nucleon flight path will greatly enhance particle identification by slightly deflecting the protons. The efficiency of HCal is expected to be very high and stable and to be well calibrated from, already approved, lower- Q^2 measurement. Projected systematic errors on the measured ratio of cross sections are 4.8% and 5.4% (corresponding to 2.4% and 2.7% on the ratio of the magnetic form factor to that of the proton). Statistical errors are projected to be smaller, allowing adequate statistics for tests of systematic effects. This proposal significantly extends the kinematics range of the already approved 12 GeV proposals E-09-019 and E12-07-104. The form factors assumed here for rate predictions are more conservative, especially at high Q^2 than the scaled dipole used in the earlier proposals. The high luminosity of the present proposal yields adequate statistics despite the reduction in cross sections. These kinematic points were originally included as part of E-09-019 but were not approved as part of that experiment.

We request a total of 16 days at a beam energy of 11. GeV.

Contents

1	Introduction	6
2	Technique	9
3	Proposed Kinematics	13
4	Apparatus	13
5	Neutron/Proton Identification	19
6	Acceptance and Fiducial Cut on \vec{q}	25
7	Nucleon Detection Efficiency	26
8	Simulations	30
8.1	Quasi-elastic	30
8.2	Inelastic	31
8.3	Inelastic Background Normalization	32
9	Inelastic Background	35
10	Rates and Trigger	41
11	Systematic Errors	42
11.1	Acceptance Losses	45
11.2	Inelastic Contamination	46
11.3	Nucleon mis-identification	46
11.4	Nucleon Detection Efficiency	46
12	Installation	47
13	Beam Time Request	47
14	Relation to Other Experiments	48
15	Group Contributions to 12 GeV Upgrade	51

1 Introduction

The elastic form factors probe the four-current distributions of the nucleons, fundamental quantities that provide one of the best opportunities to test our understanding of nucleon structure. A number of theoretical techniques exist to describe the nucleon's electromagnetic structure, including quark models, perturbative Quantum Chromo-Dynamics (pQCD), lattice QCD, effective field theories, vector-meson dominance (VMD) models, etc. Each at present has limitations, and its validity must be confirmed by experiment. In the examples given,

- quark models, as constructed, are phenomenological with no firm basis in QCD,
- pQCD is limited to high four-momentum transfer, and it is unknown at what momentum transfer it becomes valid,
- lattice QCD is presently limited, by computational requirements, to describing the isovector (proton minus neutron) form factors, since the effects of disconnected quark lines largely cancel in these,
- effective field theories are limited to small momentum transfer, and
- VMD models are constructed as fits to the existing data base.

Experimentally, the nucleon electromagnetic form factors are a central part of the Jefferson Lab 12 GeV program, and it is desirable to measure all four nucleon form factors over the widest possible Q^2 range, to similar precision. This goal is particularly motivated so that one can construct the isovector form factors for comparison with lattice calculations.

In the one-photon approximation the cross section for scattering of electrons from a spin- $\frac{1}{2}$ target can be written as

$$\frac{d\sigma}{d\Omega} = \eta \frac{\sigma_{\text{Mott}}}{1 + \tau} \left((G_E)^2 + \frac{\tau}{\epsilon} (G_M)^2 \right)$$

where

- $\eta = \frac{1}{1 + 2 \frac{E}{M_N} \sin^2(\theta/2)}$ is the recoil factor
- $\epsilon = (1 + \vec{q}^2/Q^2 \tan^2(\theta/2))^{-1} = (1 + 2(1 + \tau) \tan^2(\theta/2))^{-1}$ is the longitudinal polarization of the virtual photon,
- $\tau = Q^2/4M_N^2$, and
- $G_E(Q^2)$ and $G_M(Q^2)$ are the Sachs Electric and Magnetic form factors.

Alternately, the helicity conserving F_1 and helicity nonconserving F_2 form factors can be written as simple linear combinations of the electric G_E and magnetic G_M form factors. The measurement of these form factors for the proton and neutron probes their electromagnetic structures.

Little is known of the neutron's magnetic form factor, G_M^n , (and less of its electric form factor) for $Q^2 > 4$ (GeV/c)². *We propose to make high precision measurements of G_M^n at $Q^2 = 16.0$ and 18.0 (GeV/c)², the highest- Q^2 proposed measurements of G_M^n to date.*

Since the form factors are functions only of Q^2 , they may be separated by the Rosenbluth technique, making cross section measurements at the same Q^2 but different ϵ to obtain different linear

combinations. The apparent failure of this technique in extraction of G_E^p at $Q^2 > 1$ (GeV/c)² (as revealed by the recoil polarization method [2,3]) may indicate a failure of the one-photon exchange approximation [4]. This does not invalidate the form given above, however. It just underscores the fact that the corrections may be non-negligible and may become important particularly when trying to separate a small contribution from a larger one. This consideration does not present a great problem when trying to extract the magnetic form factor of the neutron since the electric form factor is generally much smaller, at least at low Q^2 .

These Sachs form factors are trivially related to the Dirac and Pauli form factors, F_1 and F_2 , respectively, which are the coefficients of the helicity-conserving and -nonconserving currents to which the photon can couple. Non-relativistically the Sachs form factors can be interpreted as the Fourier transforms of the charge and current distributions to which the photon couples in the target. No such simple interpretation is available at higher Q^2 . The electric form factor at any Q^2 can still be related to the Fourier transform in the Breit frame. But since the Breit frame is a different frame for each Q^2 , this relationship cannot be inverted to extract a charge distribution without a prescription for boosting the nucleon. Recent work [5] by Miller offers an interpretation of the infinite-momentum frame charge density of the nucleon as a function of impact parameter in terms of the Dirac form factor, $F_1 = (G_e + \tau G_m)/(1 + \tau)$. Interestingly, this implies that knowledge of the *magnetic* form factor of the neutron is important to the understanding of its charge distribution. Furthermore, Miller concludes that the neutron charge distribution is negative for small impact parameter, which contrasts, at least naïvely, with the long-standing belief that the neutron charge distribution is positive at the center. A positive central charge distribution is in accordance with intuitive models – for example, the neutron charge distribution reflects a virtual $p\pi^-$ pair, with the more massive proton closer to the center of mass. The interest in understanding the charge distribution is reflected by the appearance of a figure indicating the positive central charge distribution in the recent Nuclear Physics long Range Plan.

In the approximation that the strange quark does not contribute to the electromagnetic structure of the nucleon, the form factors can be combined [6–8] to extract information about the contributions of individual quark flavors to the electromagnetic structure of the nucleon. Assuming isospin symmetry, the up-quark distribution of the proton is identical to the down-quark distribution of the neutron and *vice versa*. Since the electromagnetic couplings to the individual quarks are known (and the coupling to gluons vanishes) the electric or magnetic form factor of each nucleon can be written as a linear combination of the electric and magnetic form factors of the two quark flavors. Combining measurements on the neutron and proton then allows direct extraction of the “up” form factor (including contributions from u and \bar{u} quarks from the sea, as well as valence quarks) and the “down” form factor (also composed of all d and \bar{d} contributions). In particular, improved measurements of the neutron’s magnetic form factor can be combined with measurements of the proton’s magnetic form factor to allow extraction of the “up-magnetic form factor” and “down-magnetic form factor”. If, on the other hand, the contribution of strange quarks is *not* negligible, then the measurement of the neutron form factors would be critical to allowing the strange contribution to be measured. (At present, however, there are no plans to measure strange form factors in the Q^2 range in which we propose to measure.)

The form factors are pivotal as the meeting place between theory and experiment. Calculations of nucleon structure (as opposed to parameterizations of form factors) can be tested by their ability to predict the experimentally accessible information on nucleon structure reflected in the form factors. (Of course, polarization observables and structure functions will also be relevant.) In par-

ticular, lattice QCD predictions will eventually have the capability to make meaningful predictions of hadronic structure. Form factors of the proton and neutron will present important tests of those predictions.

A great deal of experimental and theoretical effort [9–11] is being expended on an ambitious effort to greatly expand the knowledge of nucleon structure by determining the generalized parton distributions. Measurement of form factors plays an important role in that effort since the form factors set the values of sum rules which the generalized parton distributions must obey.

The neutron’s form factors are more difficult to measure, of course, because there is no free-neutron target. Spin-asymmetry techniques have been used in extracting the tiny electric form factor of the neutron [12–18] and also in measuring the magnetic [19–21] form factor, particularly at low Q^2 . Generally at high Q^2 , however, quasielastic scattering from the deuteron has been used [22–37] to extract G_M^n . This is based on the fact that the deuteron is a loosely coupled system, so high- Q^2 quasi-elastic scattering can be viewed as the sum of scattering from a proton target and scattering from a neutron target. This simple picture is complicated only slightly by the fact that the targets are not at rest but are moving with the “Fermi motion” intrinsic to the deuteron’s wave-function.

Several techniques have been used to try to isolate the electron-neutron scattering of interest. In the “proton-subtraction” technique [22–27] single-arm quasi-elastic electron scattering from the deuteron is measured. This is combined with a measurement of single-arm elastic scattering from the proton. An attempt is made to fold in the expected effects of Fermi motion to simulate the expected contribution of the proton in the measured quasi-elastic spectrum. This is then subtracted and the remainder is interpreted as a measure of quasi-elastic electron scattering off the neutron from which the (almost purely magnetic) form factor can be determined. This technique tends to suffer from the error-propagation problems intrinsic to subtraction of two large numbers. At low Q^2 the proton electric form factor dominates (and the proton magnetic form factor is never small compared to the neutron’s). At high Q^2 inelastic background becomes a serious problem, to the extent that the quasi-elastic “peak” may not be visible, even as a shoulder on the background peak. Because these are single-arm measurements, no other information is available with which to selectively reject background events.

The “proton-tagging” technique [28, 29] is a partial-coincidence method which takes advantage of the fact that protons are easier to detect than neutrons. In that technique quasi-elastic electron scattering is measured with an additional charged-particle detector centered around the direction of the momentum-transfer vector, \vec{q} . If no proton is detected, the event is ascribed to scattering from the neutron. This technique generally requires substantial theory-based corrections to account for the tail of the Fermi-motion which would cause a recoil proton to miss the charged-particle detector (or cause a spectator proton to hit it). Again, since the neutron is not detected, no cuts can be applied to selectively reject inelastic background events.

We propose to use the “ratio-method” [39] which is discussed in detail in the next section. It relies on measurement of both the recoil protons and recoil neutrons [30–37]. Inelastic background is substantially suppressed by even a crude nucleon-coincidence requirement. As will be seen in simulations presented in section 9, precise measurement of the final-nucleon direction permits the use of cuts which further reduce inelastic background down to manageable levels, even at the highest Q^2 . If the particle detection, particularly the neutron detection is well understood, this technique is subject to the smallest systematic errors as it enjoys substantial cancellation of many sources of systematic error which plague other techniques.

There are relatively few measurements of G_M^n beyond $Q^2 = 1$ (GeV/c)². The few published measurements in the range $1 < Q^2 < 4.5$ (GeV/c)² (shown in Fig. 1) have been eclipsed, both in number of points and in precision, by the recent CLAS data [37, 40] of Lachniet. These data are shown in Fig. 1 as the blue points. Several of the proposers of the present experiment played key roles in the CLAS experiment (Quinn, Brooks and Gilfoyle). The ratio-method was used for those measurements and will be used in the proposed experiment.

In the figure, the value of G_M^n is divided by the ‘scaled dipole’. The dipole is a vector-meson-dominance-inspired empirical parameterization of the proton’s electric form factor: $G_E^p \approx G_D = (1 + Q^2/.71 \text{ (GeV/c)}^2)^{-2}$. This appeared to be a good approximation for G_E^p over a large Q^2 range until recent recoil-polarization measurements [2, 3]) showed that G_E^p actually fell rapidly below the dipole form for $Q^2 > 1$ (GeV/c)². The scaling approximation hypothesizes that $G_M^p \approx \mu_p G_D$ and $G_M^n \approx \mu_n G_D$. The CLAS data show that the ‘scaled dipole’ is a surprisingly good approximation for G_M^n out to $Q^2 \approx 4.5$ (GeV/c)².

Beyond $Q^2 = 4.5$ (GeV/c)² there are only a few points, with large errors. The solid green points in Fig. 1 are SLAC measurements [26] made using the “proton-subtraction” technique. While these points have relatively large errors, they point to a trend which is not seen in the CLAS data. This makes it particularly interesting to investigate the behavior of G_M^n in the range $Q^2 > 4$ (GeV/c)² with a measurement which is independent of either of those shown in Fig. 1. A similar plot is presented at the end of the proposal, with the projected errors of the proposed measurement superimposed. The scaled-dipole approximation is shown in the figure, as a horizontal line at exactly 1, and a more recent parameterization [38] of nucleon form factors is shown in violet.

2 Technique

We propose to use the “ratio method” [39] to determine G_M^n from quasi-elastic electron scattering on the deuteron for $Q^2 = 16$ and 18 (GeV/c)². This method is far less sensitive to systematic errors than the “proton-subtraction” or “proton-tagging” techniques.

Use of the “ratio method” requires the measurement of both neutron-tagged, $d(e, e'n)$, and proton-tagged, $d(e, e'p)$, quasi-elastic scattering from the deuteron. Simultaneous measurements of both these reactions provides a substantial reduction of systematic error because numerous experimental uncertainties cancel in forming the ratio:

$$R'' = \frac{\frac{d\sigma}{d\Omega} |_{d(e, e'n)}}{\frac{d\sigma}{d\Omega} |_{d(e, e'p)}} \quad (1)$$

This is insensitive, for example, to target thickness, beam intensity, deadtime, electron trigger efficiency, electron acceptance, and the detection and reconstruction efficiency for the scattered electron track.

With a small and accurately-calculable nuclear correction, ϵ_{nuc} , this measured ratio of quasi-elastic cross sections can be used to determine the ratio of the elastic cross sections:

$$R' = \frac{\frac{d\sigma}{d\Omega} |_{n(e, e')}}{\frac{d\sigma}{d\Omega} |_{p(e, e')}} = \frac{R''}{1 + \epsilon_{\text{nuc}}}$$

Because of final-state interactions and other nuclear effects, there would be substantial corrections to the naïve assumption that the coincident quasi-elastic cross section is equal to the cross section for

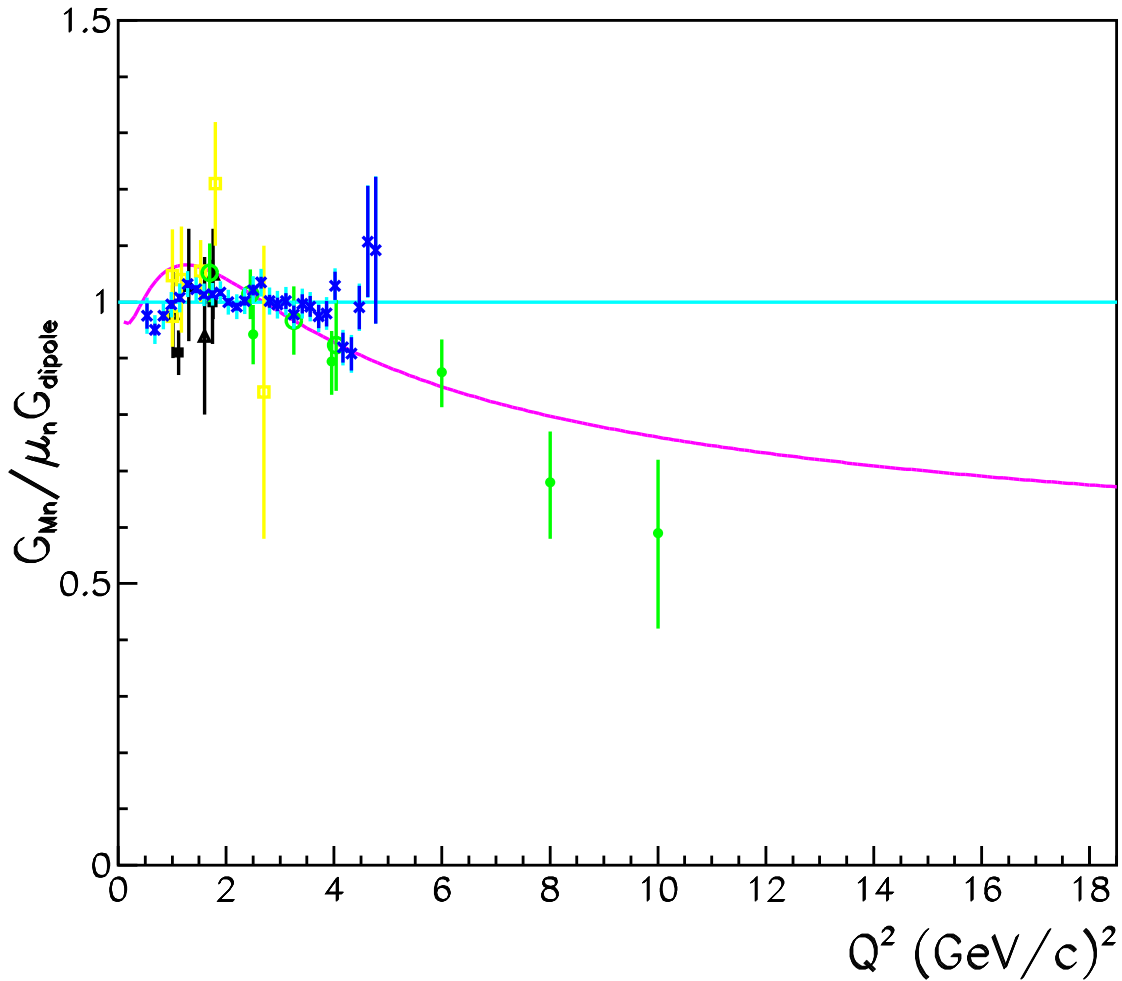


Figure 1: Existing data on G_M^n in $Q^2 > 1$ $(\text{GeV}/c)^2$ range are plotted as ratio to scaled dipole approximation. Blue points are from CLAS e5 run [37,40]. Dark blue lines show the statistical error while light blue extensions show the quadrature sum of statistical and systematic errors. Solid green circle [26] and hollow green circle [27] points are from SLAC. Older data are shown as yellow squares [31], black squares [29], and black triangles [25]. Some points have been slightly displaced horizontally to avoid overlap. The light blue horizontal line represents the scaled-dipole parameterization while the violet curve shows a recent parameterization [38]

elastic scattering from the free nucleon. Further, these corrections would depend upon the fraction of the quasi-elastic peak which is integrated. A great advantage of the ratio method (with a deuteron target) lies in the fact that these corrections are almost identical for the case of the neutron and the proton and so they cancel almost completely in the ratio. The small surviving correction, ϵ_{nuc} , to the ratio arises due to small effects such as the neutron-proton mass difference. Figure 2 shows detailed calculations [42] by Arenhövel of the correction factor required in calculating the ratio of the nucleon elastic cross sections from the ratio of the integrated nucleon-tagged quasi-elastic cross sections. Here θ_{pq} is the angle between the struck nucleon's final momentum vector (\vec{p}) and the momentum-transfer vector (\vec{q}). Final state interaction effects are minimized by putting a tight cut on θ_{pq} (i.e. requiring that the nucleon actually recoil in the direction which would be expected in the absence of Fermi motion and final state interactions). It will be seen below that the region of interest in the present proposal has $\theta_{pq} < 1$ degree. Even at $Q^2 = 1.2$ (GeV/c)² the correction is seen to be less than 1%. For higher Q^2 up to 5 (GeV/c)² calculations of the nuclear correction have been made [37, 40] using a model [43] which applies Glauber theory to model the final-state interactions. Again, the corrections for the neutron and proton are almost identical and cancel in the ratio. The residual correction on the ratio ϵ_{nuc} was found to be under 0.1%. The corrections are expected to be very small and calculable in the range of interest here. This correction is expected to contribute negligibly to the systematic error of the measurement.

Writing R' in terms of neutron form factors,

$$R' = \frac{\eta \frac{\sigma_{\text{Mott}}}{1+\tau} ((G_E^n)^2 + \frac{\tau}{\epsilon} (G_M^n)^2)}{\frac{d\sigma}{d\Omega} \Big|_{\text{p}(e,e')}}}$$

where η , ϵ , and τ are defined above.

From this, then, can be extracted the ratio of interest,

$$R = R' - \frac{\eta \frac{\sigma_{\text{Mott}}}{1+\tau} (G_E^n)^2}{\frac{d\sigma}{d\Omega} \Big|_{\text{p}(e,e')}}} = \frac{\eta \sigma_{\text{Mott}} \frac{\tau/\epsilon}{1+\tau} (G_M^n)^2}{\frac{d\sigma}{d\Omega} \Big|_{\text{p}(e,e')}}} \quad (2)$$

The term subtracted to extract R from R' will be small ($\approx 1\%$ at most, and much less at high Q^2) if G_E^n follows the form of the Galster parameterization. In section 11 we will allow for an error of 400% of Galster and find that this correction still does not cause unacceptable systematic errors. A measurement of G_E^n up to $Q^2 = 10$ (GeV/c)² is planned [41] in a time-frame which will make it useful for analysis of results from this measurement.

This measurement of R then allows G_M^n to be determined, given just the proton's elastic cross-section at the corresponding kinematics. It may be noted that, because R is proportional to the square of G_M^n , the fractional error on G_M^n will actually be only half of the fractional error on R . Since the quantity of greatest interest is G_M^n , it is conventional to report the expected size of the errors on G_M^n . However, the experiment will actually be a direct measurement of R'' (from which R is inferred with small corrections, as described above). This distinction is significant only in that present uncertainties on the proton's form factors (and cross section) do not actually imply systematic errors on the quantity being measured, R'' (or R). Subsequent improvements in the determination of the proton cross section, at the kinematics of interest, can be combined retrospectively with the results for R from this measurement to obtain improved values for G_M^n . There would be no need to repeat the analysis of this experiment to incorporate new proton measurements.

Ratio correction factor from Arenhoevel calculation

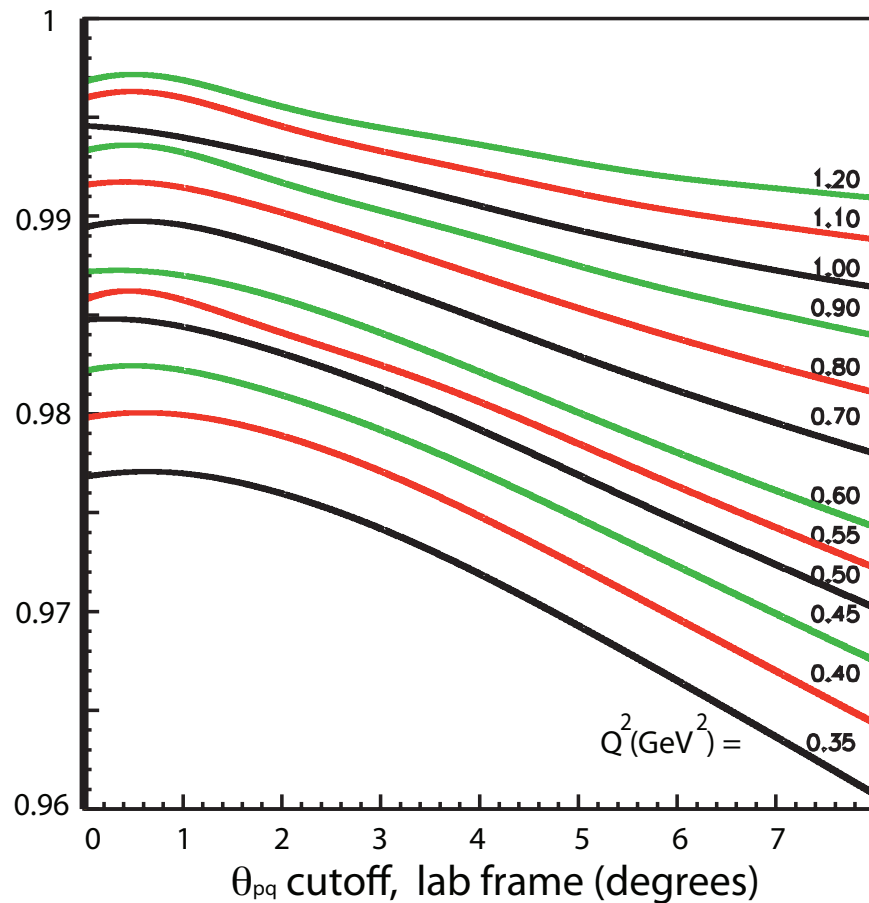


Figure 2: Arenhövel predictions for (low Q^2) nuclear corrections (including FSI) as a function of the maximum accepted value of θ_{pq} . The required correction is seen to be small for tight cuts on θ_{pq} and to *decrease* with increasing Q^2 .

Table 1: Kinematics of proposed measurements are shown below the double line while those of E-09-019 are shown above.

Q^2 (GeV/c) ²	E_{beam} (GeV)	θ_e	θ_N	E' (GeV)	P_N (GeV/c)
3.5	4.4	32.5°	31.1°	2.5	2.6
4.5	4.4	41.9°	24.7°	2.0	3.2
6.	4.4	64.3°	15.6°	1.2	4.0
8.5	6.6	46.5°	16.2°	2.1	5.4
10.	8.8	33.3°	17.9°	3.5	6.2
12.	8.8	44.2°	13.3°	2.4	7.3
13.5	8.8	58.5°	9.8°	1.6	8.1
16.	11.	45.1°	10.7°	2.5	9.4
18.	11.	65.2°	7.0°	1.4	10.5

Similarly, since the proton cross section is dominated by G_M^p for these kinematics, the ratio of form factors, G_M^n/G_M^p can be cleanly extracted from the data. In many ways this ratio is more fundamental than G_M^n , lending itself to direct comparison to theoretical predictions. Extraction of this ratio does not suffer from a systematic error due to uncertainties in proton cross section measurements. Like G_M^n , this ratio enjoys a factor of two reduction in the fractional error compared to R .

3 Proposed Kinematics

The two kinematic points at which we propose to measure are shown in Table 1 along with the seven approved kinematic points of E-09-019. The lowest- Q^2 points will overlap with existing CLAS measurements while the highest- Q^2 points will greatly extend the range in which G_M^n is known with high precision

While the scattered electron energy is relatively constant (mostly near 1 to 2 GeV) across the kinematic points, the central nucleon momentum of interest is seen to vary from 2.65 GeV/c to 10.5 GeV/c. Individual calibrations with 'tagged' protons and 'tagged' neutrons will be carried out at low- Q^2 kinematic points to ensure that the neutron and proton detection efficiencies are well known. As will be seen below, the efficiencies are large and stable for higher Q^2 . Tagged proton calibrations are also planned at these high- Q^2 points.

4 Apparatus

The use of the ratio method depends upon detection of both scattered neutrons and protons. Potential sources of systematic error arise in determining the acceptance and detection efficiency of these particles. Errors associated with nucleon acceptance can be reduced by matching the neutron and proton acceptances so they cancel in the ratio (as does the electron acceptance and efficiency).

Neutron Magnetic Form Factor at $Q^2 = 18 \text{ GeV}^2$

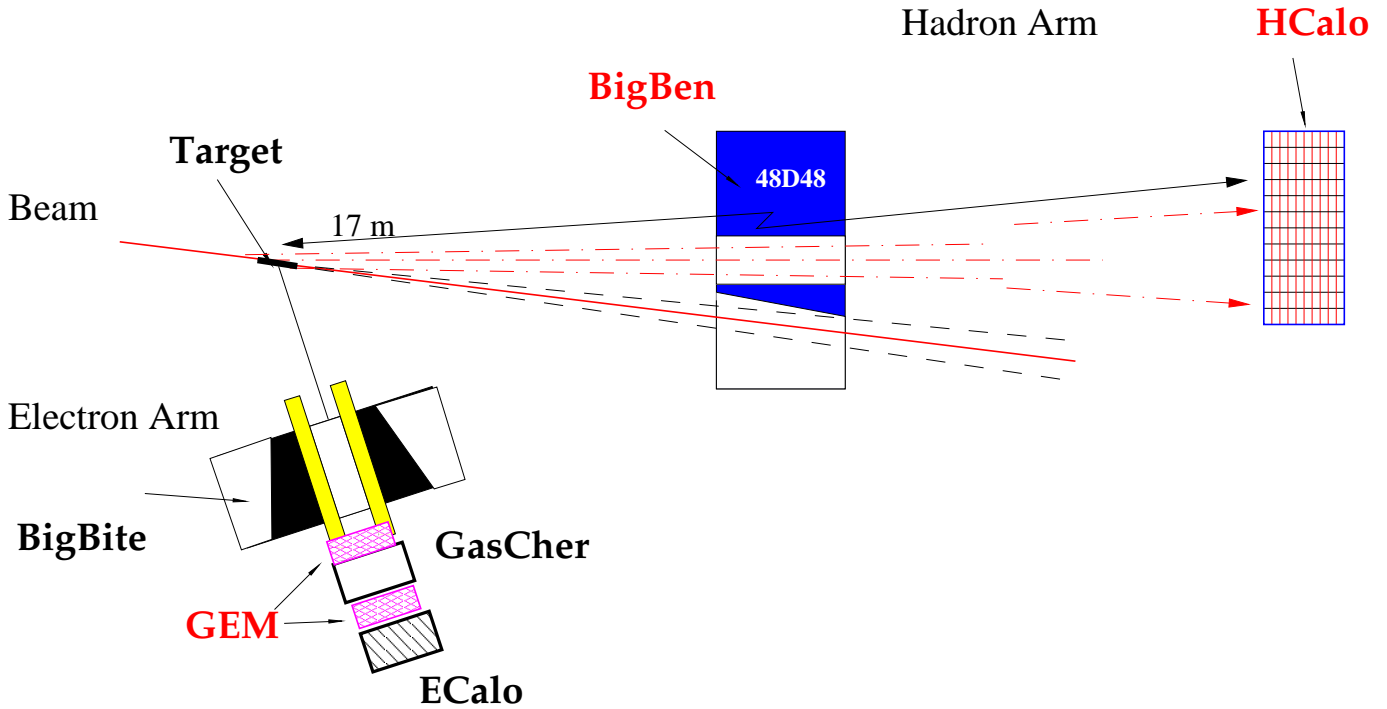


Figure 3: A schematic view of the apparatus is shown as configured for the higher Q^2 point. BigBite will detect scattered electrons while HCal will detect the scattered nucleons. The dipole magnet “BigBen” will deflect protons for the purpose of particle identification. A magnetically-shielded hole in the return iron will allow the unscattered beam to continue on to the beam dump. Corrector coils (not shown) will compensate for any effect of residual magnetic field on the beamline. Note: the 17 m flight path to HCal is not drawn to scale.

We propose to use the existing BigBite spectrometer (with modified instrumentation) in Hall A to measure the momentum and angle of the scattered electrons and the HCal hadron calorimeter to detect both the scattered neutrons and protons. The use of HCal in place of the BigHAND detector array is a major improvement from the technique originally proposed for E-09-019. Nucleons scattered toward the HCal will pass through the field of a large aperture dipole magnet which will be positioned along the nucleon flight path to vertically deflect protons relative to neutrons. The layout of the experiment is shown schematically in Fig. 3.

The targets will be 10 cm long liquid deuterium (and liquid hydrogen for calibration) cells with 100 μm aluminum windows. This gives about 1.7 g/cm^2 of target compared to about 0.054 g/cm^2 in the windows. As discussed below, selection cuts will reduce the contribution of quasi-elastic events from aluminum below this 3.2% ratio. To obtain percent-level precision, however, it will be necessary to subtract the contribution from the windows. A dummy target cell will be used, having windows at the same position as the real cell but with windows thick enough to give the same luminosity as for a full cell. Sufficient statistics for subtraction of the windows will be obtained by

running on the dummy cell for about four percent of the beam time used for the full target.

As discussed below, past experience combined with simulation suggests the BigBite and HCal rates will be reasonable at a luminosity of $2.8 \times 10^{38}/A$ /cm²/s where A is the number of nucleons in the target. This is four times higher luminosity that was considered prudent in the originally proposed E-09-019, using BigHAND scintillator array for nucleon detection. For a luminosity of 1.4×10^{38} /cm²/s on a 10 cm deuterium target, the beam current would be 44 μ A.

BigBite, shown in Fig. 4, is a large acceptance non-focusing magnetic spectrometer. It has a large acceptance (roughly 53 msr in the intended configuration) and has been used successfully at high luminosity ($\approx 10^{37}$ /cm²/s). It will be configured for high momentum measurements, with the entrance aperture of the dipole 1.55 m from the target and widely spaced coordinate-measuring detector planes. For the high luminosity of the experiment, the spectrometer will be instrumented with GEM detector planes. These detectors are planned for use in the tracking and polarimeter of the new Super BigBite Spectrometer (SBS) and so will be available for use as the tracking detectors for BigBite. The GEM detectors have been designed so the same modules can be used to instrument the BigBite spectrometer or the new SBS spectrometer. The modules being designed for use as forward trackers for SBS (shown in Fig. 5) will also serve as the front detector planes for BigBite. Similarly, the modules designed for use in the SBS polarimeter (shown in Fig. 6) will be of suitable size to serve at BigBite's back detector planes. In this configuration, the expected momentum resolution will be $\sigma_p/p \approx .5\%$ because of the high resolution and small multiple-scattering resulting from the relatively thin GEM detectors. The angular resolution is expected to be better than 1 mr in both horizontal and vertical angles [46].

We intend to run with a trigger based upon the electron spectrometer with a very loose trigger-level coincidence requirement from HCal. Both the coincidence time window and the HCal threshold will be set very wide compared to the cuts to be used in analysis. This, combined with the very similar response of HCal to neutrons and protons at the momentum of interest, eliminates any neutron/proton bias from the trigger and ensures that the trigger efficiency cancels in the ratio of interest, R. Additionally, a prescaled fraction of single-arm BigBite triggers will be accepted. The lead-glass electromagnetic calorimeter will be used for the BigBite trigger. As will be discussed in section 10, this is expected to allow a modest trigger rate of less than 1 kHz. If the gas Cerenkov has been successfully commissioned, it may also be used for redundant rejection of pions in BigBite.

The HCal is an iron-scintillator sampling hadron calorimeter which will be built for the SBS spectrometer. It is based on the design [47] of a calorimeter used at COMPASS at CERN. The design of the calorimeter may still be optimized for the JLab environment but the performance is expected to be at least as good as the starting design, which was used for simulations. The calorimeter consists of 15 cm \times 15 cm modules with a thickness of 4.8 interaction lengths (1.01 m thick) of 40 alternating layers of iron and scintillator. The scintillators are read out by a wavelength shifter running along one side of the module. The planned calorimeter will consist of an array of 11 modules horizontally \times 22 modules vertically. Two independent simulations of the modules have been done. One simulation [48], using Geant 3, was used extensively for background studies but also looked at detection efficiency [49] as a function of threshold. An example event, and the environment simulated, is shown in Fig. 7. The other simulation [50, 51], using Geant 4, to simulate the entire 11 \times 22 array, was used for more extensive studies of resolution and clustering algorithms as well as additional efficiency studies.

Results for predicted spatial resolution are shown in Fig. 8. At the energies of interest they are significantly better than the spatial resolution which could be achieved with the originally-proposed

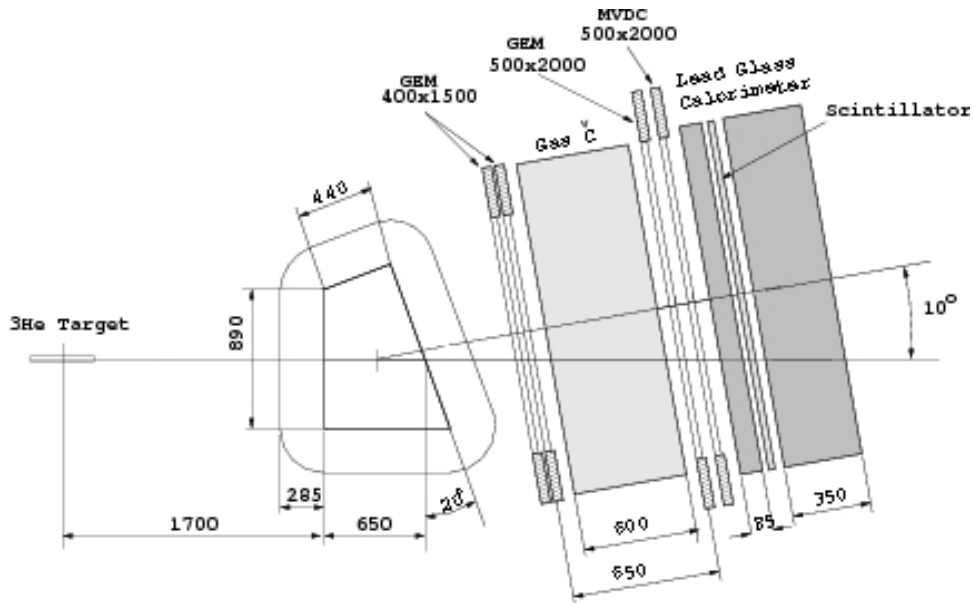


Figure 4: The BigBite spectrometer, configured for high momentum, high luminosity running. Tracking is performed with GEM detectors and a gas Cerenkov counter is located between the detector packages. (The target label refers to another experiment.)

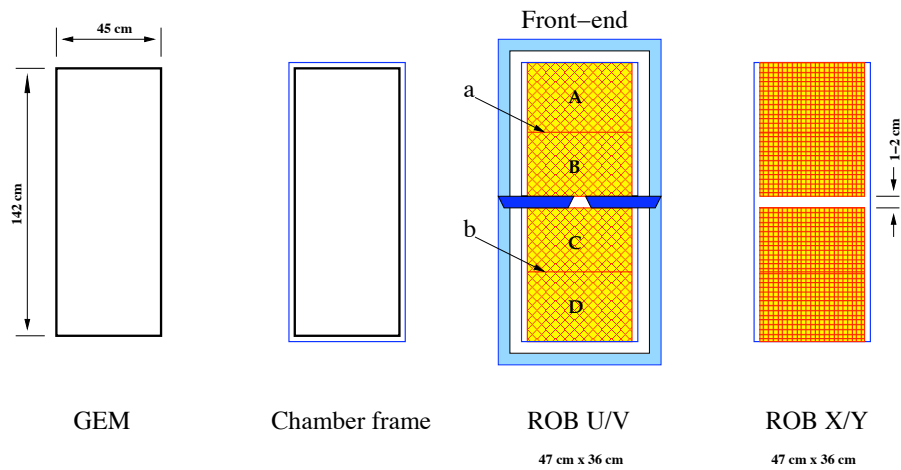


Figure 5: Outline shows the dimensions of the GEM detectors being designed as the front tracking detectors for SBS. Their size is excellent for use as the front detectors of BigByte. Also shown are some details of the read-out boards (ROBs) which will instrument the detectors.

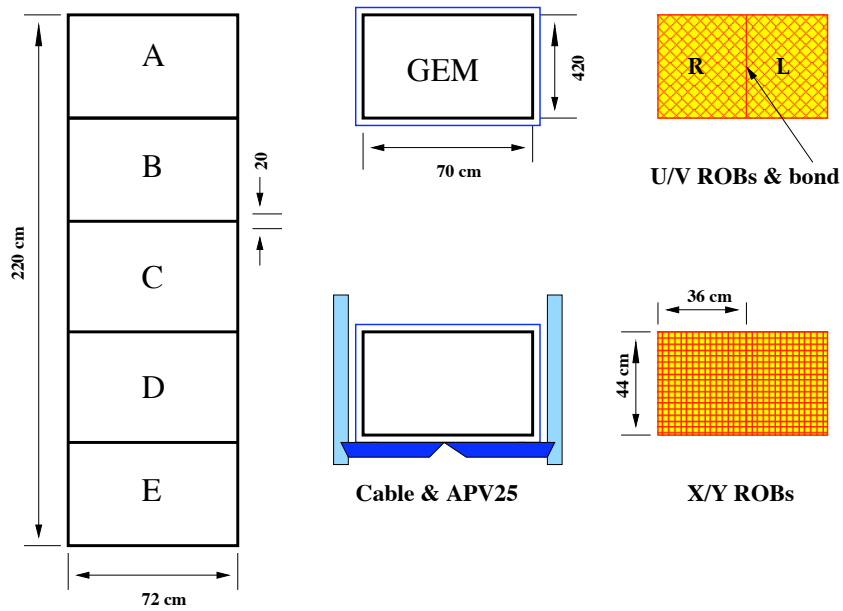


Figure 6: Outline shows the dimensions of the GEM detectors being designed as instrumentation for the polarimeter for SBS. Their size is excellent for use as the back detectors of BigByte. Also shown are the modules from which the detector planes will be constructed and some details of the read-out boards (ROBs) which will instrument the detectors.

HCAL Setup GEANT3/DINREG Model: a Neutron Interaction

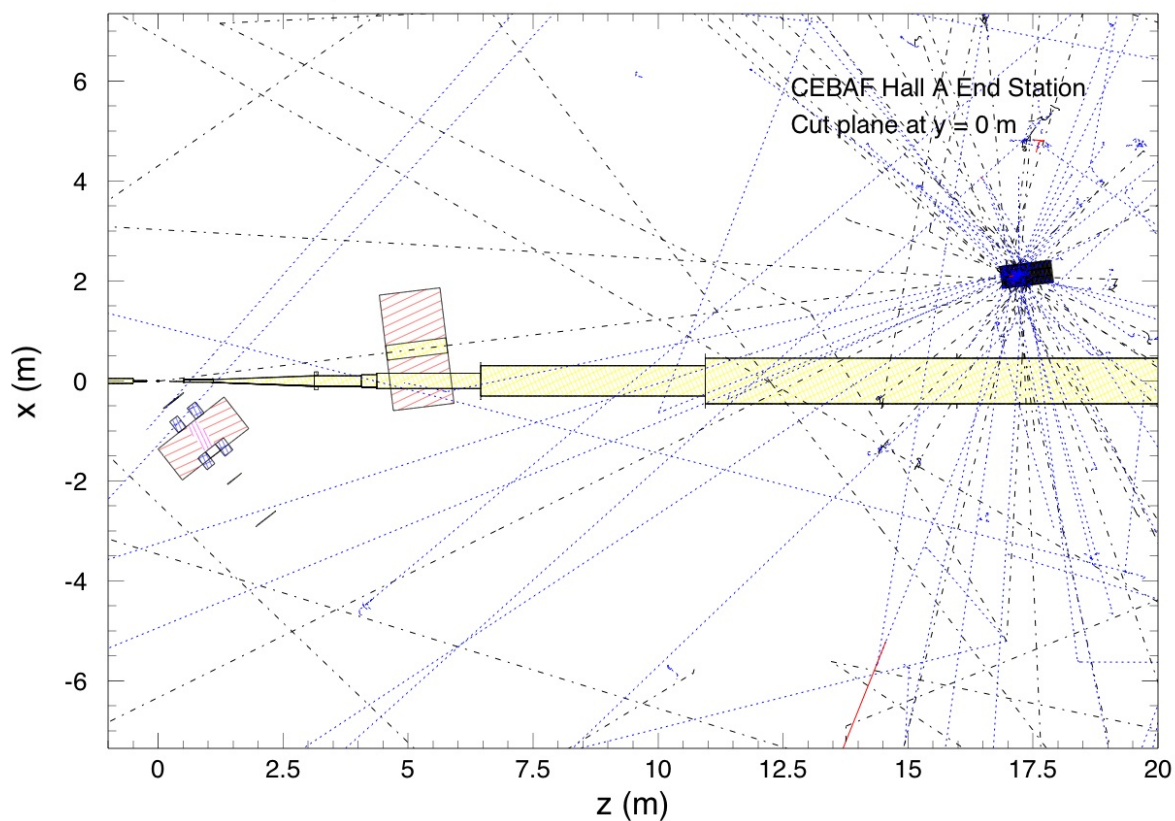


Figure 7: A neutron-detection event simulated using Geant3 [48] at the $Q^2 = 18$ (GeV/c) 2 kinematics. A 3×3 array of modules was simulated. The many escaping tracks are mostly low energy neutrons and photons (most of which would normally deposit their energy in adjacent modules).

BigHAND detector array. For the 9.4 and 10.5 GeV/c nucleons of interest, the RMS resolution (in both x- and y-directions) is ≈ 3.0 cm for protons and ≈ 3.1 cm for neutrons. The detector will be located 17 meters from the target so the corresponding angular resolution will be better than 1.8 mr ($\approx 0.1^\circ$) both horizontally and vertically. This excellent resolution will permit critical cuts on the direction of the recoil nucleon relative to the \vec{q} -vector direction.

Because of the very large amount of energy deposited in the scintillators (≈ 250 MeV), the r.m.s. time-of-flight resolution of the overall detector array is expected to be well under 1 ns. Since the momenta of the nucleons of interest are sharply defined, this will allow tight timing cuts to reject accidentals. With a 17 meter flight path, this will allow clean rejection of low energy nucleons from break-up of nuclei.

The efficiency predicted by simulation [51] for conversion and detection of neutrons and protons is shown in Fig. 9 for the $Q^2 = 16$ (GeV/c)² kinematics in Fig. 10 for the $Q^2 = 18$ (GeV/c)² kinematics. The efficiencies are seen to be excellent. At the momenta of interest, the efficiencies for neutrons are over 95.5% and are about 1% higher for protons. The inefficiencies are significantly smaller than would have been achieved with the originally proposed BigHAND. The high efficiencies and the fact that they are well matched for protons and neutrons are very advantageous in controlling systematic errors. The efficiencies are expected to be very stable (and accurately simulated) because they depend mostly on the probability of a hadronic shower being initiated rather than being sensitive to the details of energy deposition.

As described in the next section, a magnetic 'kick' will be used to distinguish protons from neutrons. We have identified a large-aperture magnet at Brookhaven National Laboratory to be used for this purpose. This same dipole will serve as the spectrometer magnet for the Super BigBite spectrometer. In its present configuration, this "48D48" magnet, shown in Fig. 11 has a 120 cm \times 120 cm (48 in. \times 48 in.) pole face with a 47 cm gap.

The magnet will be modified so it can be positioned near the beam line. This will involve machining a hole through the return yoke to provide a low-field, iron-free region for passage of the outgoing beam. Asymmetric field coils will be needed to avoid interfering with the outgoing beam. One possible solution, Correcting coils would be used to compensate for beam steering due to any residual fields.

The details of the yoke hole, field coils, field clamps, and correcting coils will be finalized using a magnetic field simulation program such as TOSCA. The magnet modifications will be designed such that the magnet can also be used for the recently-approved high- Q^2 proton elastic cross section experiment [57].

5 Neutron/Proton Identification

An obvious approach to determination of nucleon identity would be to place a thin scintillator layer upstream of the calorimeter to determine whether the incident particle is charged. This would be complicated by the need for heavy shielding between this PID layer and the target. If neutron/proton identification were based solely upon the response of such a PID layer, then contamination by mis-identification would be a significant problem. Experience from the GEN experiment [44] indicates that about 2.5% of (independently identified) protons fail to fire such a layer and would be mis-identified as neutrons [45]. More troublesome is the fact that a significant fraction ($\approx 40\%$) of the detected neutrons actually fire the veto layer (because the hadronic shower

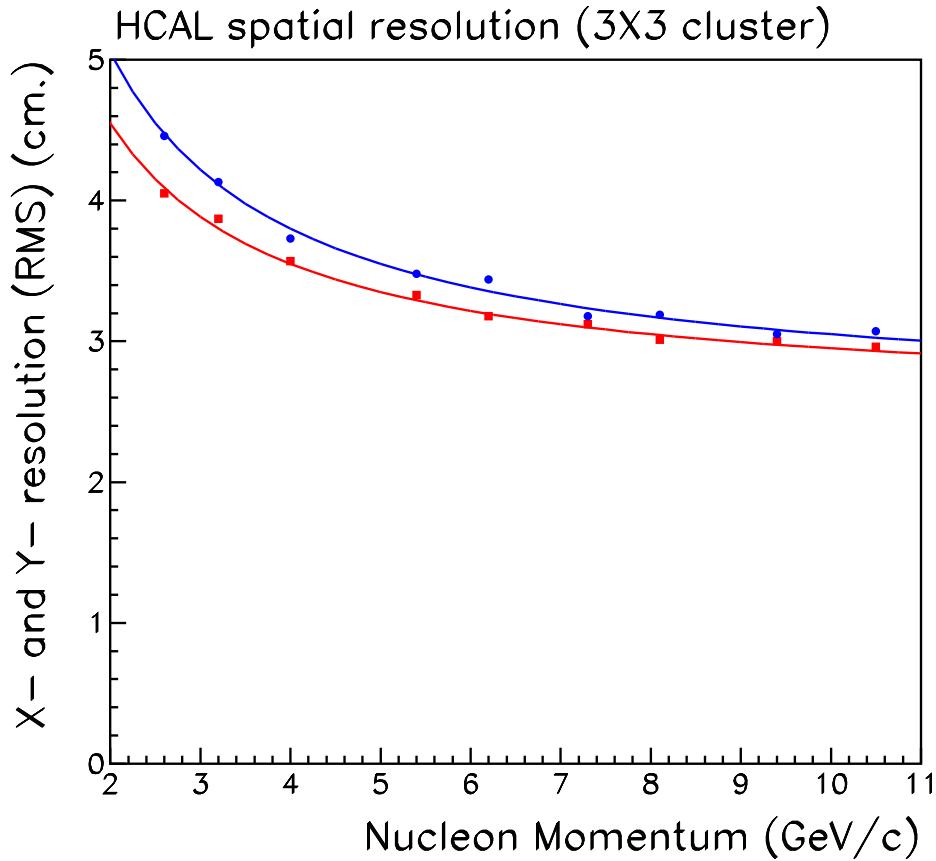


Figure 8: The predicted spatial resolution [51] as a function of nucleon momentum is shown for neutrons (blue) and protons (red). The algorithm uses only a 3×3 array of modules centered on the module with greatest light output. The position is found as the \sqrt{E} -weighted mean in both x and y. Also shown are simple fits used for simulation of background and signal.

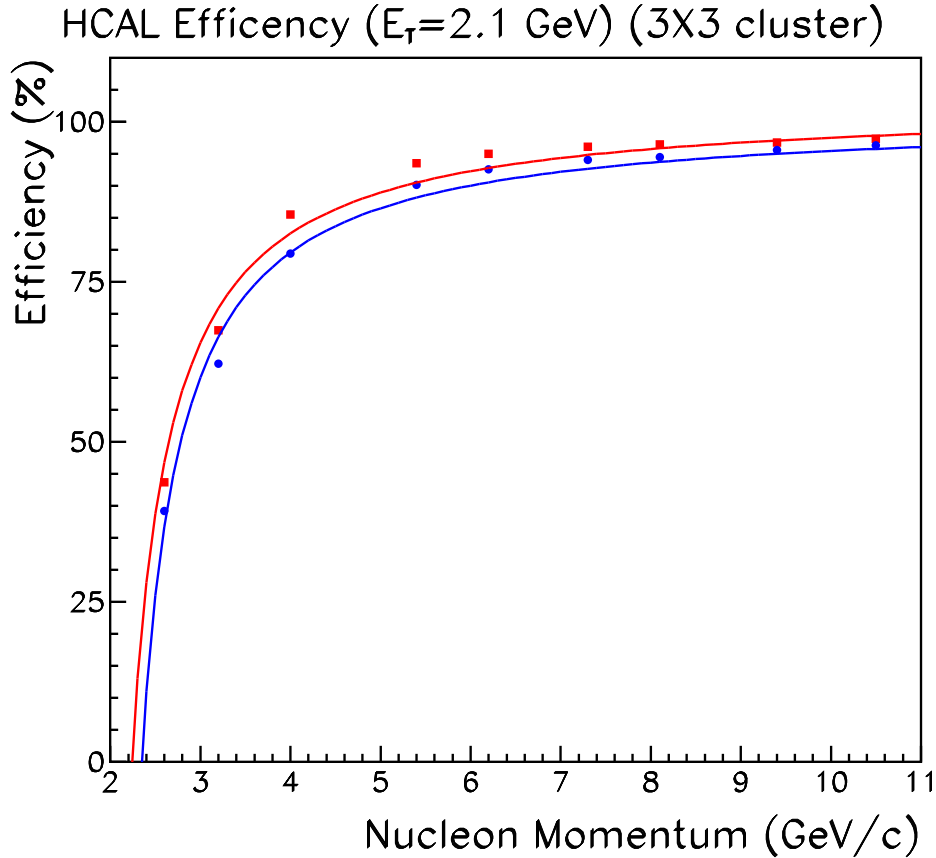


Figure 9: The predicted detection efficiency [51] as a function of nucleon momentum for the $Q^2 = 16$ $(\text{GeV}/c)^2$ kinematics is shown for neutrons (blue) and protons (red). The algorithm uses only a 3×3 array of modules centered on the module with greatest light output. The nucleons of interest have a momentum of $9.4 \text{ GeV}/c$ and a threshold of one quarter of the mean energy deposited has been assumed. Also shown are simple fits used for the purpose of background simulation.

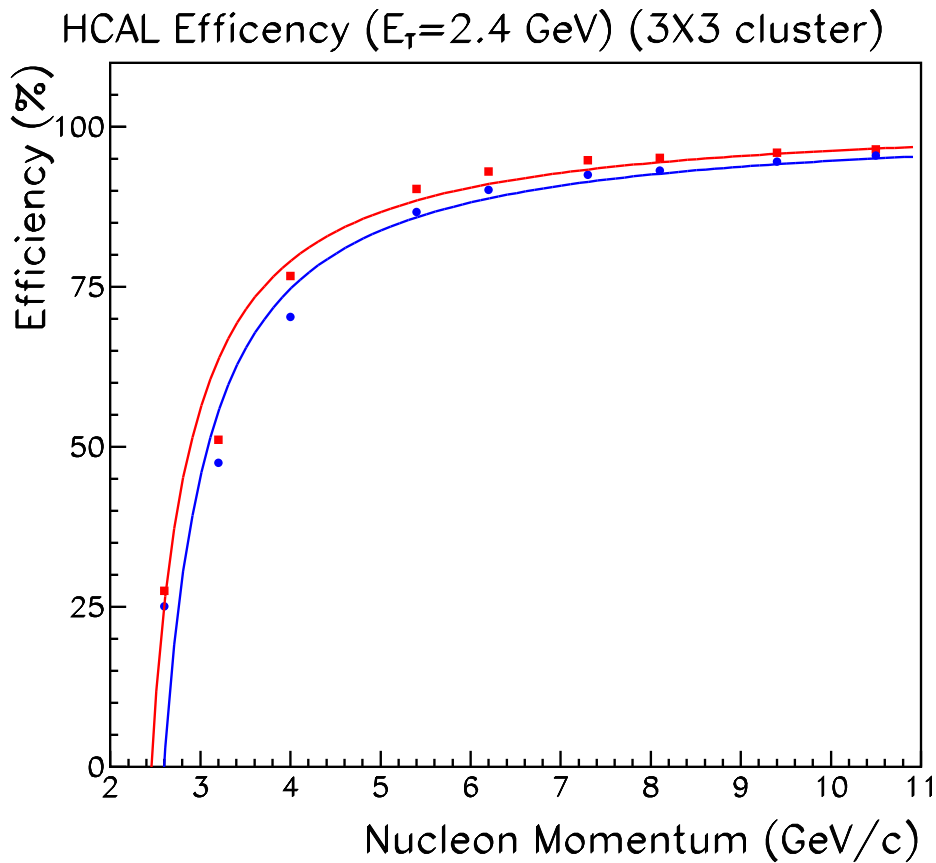


Figure 10: The predicted detection efficiency [51] as a function of nucleon momentum for the $Q^2 = 18$ $(\text{GeV}/c)^2$ kinematics is shown for neutrons (blue) and protons (red). The algorithm uses only a 3×3 array of modules centered on the module with greatest light output. The nucleons of interest have a momentum of 10.5 GeV/c and a threshold of one quarter of the mean energy deposited has been assumed. Also shown are simple fits used for the purpose of background simulation.

Table 2: Field strength for deflection dipole is given for each of the proposed kinematics. Also given are Δ_{pn} , the separation on HCal between an undeflected neutron and a deflected proton having the same \vec{q} -vector, and P_{kick} , the effective vertical momentum 'kick' given by the dipole.

Q^2 (GeV/c) ²	16.	18.
$\int Bdl$ (T-m)	1.60	1.88
Δ_{pn} (cm)	68	68
p_{kick} (MeV/c)	376	442

is initiated in the front shielding).

A much more clean separation of neutrons from protons can be made, without loss of efficiency, by introducing a dipole magnet to deflect the protons vertically. If the initial direction of the nucleon could be accurately predicted, then only a small deflection would be needed to distinguish charged particles from neutral ones. In the case of quasi-elastic scattering, the measured \vec{q} -vector does not precisely predict the direction of the struck nucleon's final momentum since the initial momentum of the nucleon within the deuteron also contributes. Using a reasonable model of the deuteron's wave-function [56], the momentum distribution can be determined. It is found that, with 95% probability, the component of the nucleon's momentum along any chosen direction is less than 100 MeV/c. A magnetic 'kick' of 200 MeV/c, then would separate quasi-elastic protons from neutrons at the 95% level. In the simplest analysis, a horizontal line could be defined across the face of HCal (for any given event detected in BigBite) such that the struck nucleon would have a 95% probability of falling below the line if the particle were a neutron and a 95% probability of falling above the line if the particle were a proton. Because of the high momenta of interest for the present measurements, we are able to apply almost twice as large a 'kick' (>360 MeV/c) without deflecting the protons beyond the geometric limits set by the size of HCal. Thus this source of mis-identification due to Fermi motion is reduced to nearly negligible levels.

Since the initial momenta of the nucleons are vertically symmetric, the actual distributions of neutron and proton events can be empirically determined by observing the distributions of those neutrons which are displaced downward from the point predicted for elastic kinematics and those protons which are displaced upwards from the (magnetically deflected) point predicted for elastic kinematics. This will serve to measure, and correct if necessary, any contamination due to higher-order effects such as hard final-state interactions.

A 200 MeV/c kick required to separate quasi-elastic protons from neutrons could be achieved by applying a dipole field, near the beginning of the flight path, having a field integral of $\int Bdl \approx 0.85$ T·m. For these high Q^2 kinematics, a 200 MeV/c kick would give a relatively small spatial separation on the HCal detectors. A proportionally larger field will be used to ensure an adequate displacement. Table 2 gives the field integrals assumed in the Monte Carlo simulations presented below. Also given are the resulting mean separations between the undeflected neutrons and the deflected protons.

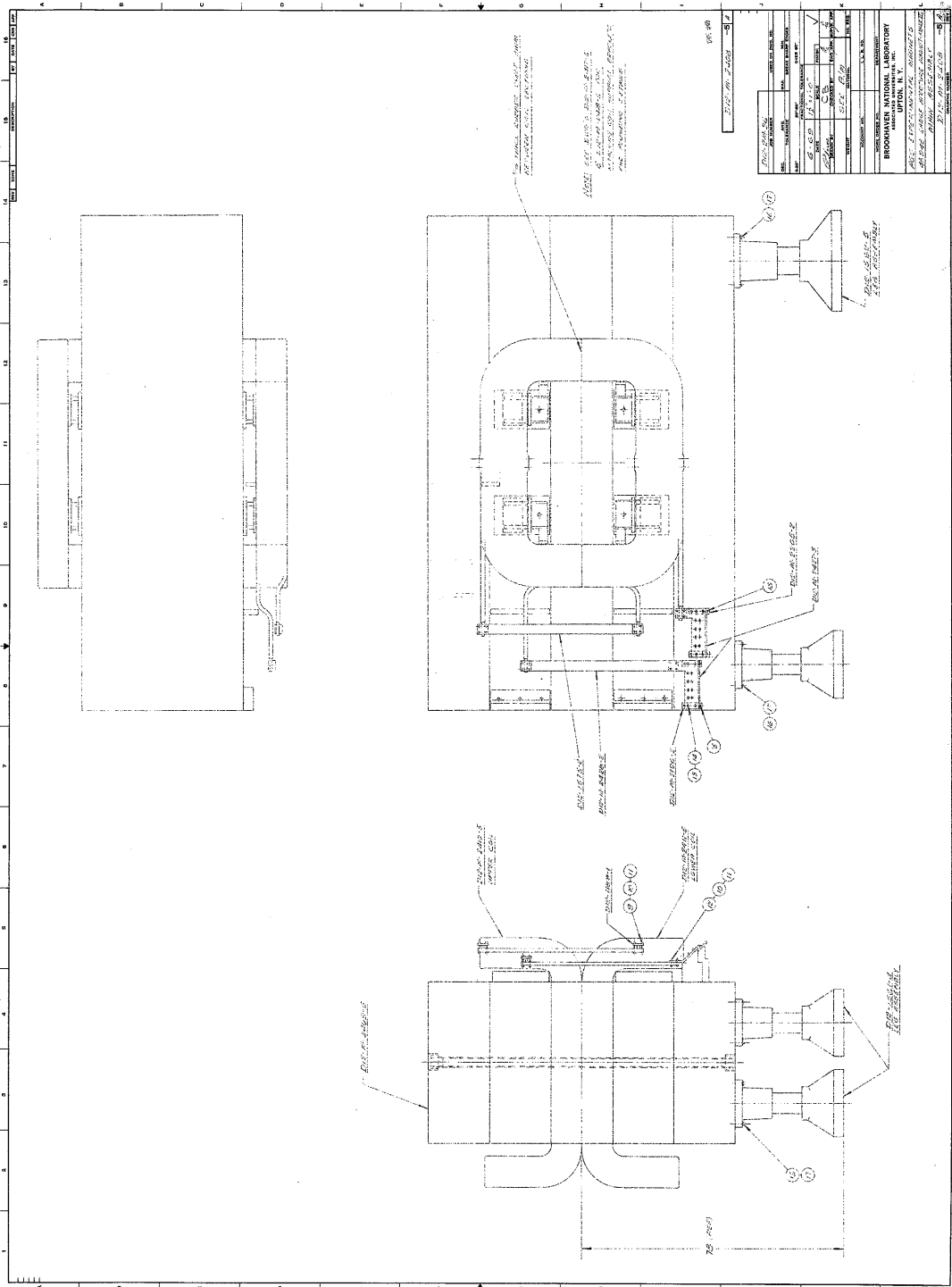


Figure 11: Assembly diagram for generic 48D48 spectrometer magnet. Magnet is shown mounted for horizontal bend-plane but will be used for vertical bend plane. Coil configuration shown is that used at BNL.

6 Acceptance and Fiducial Cut on \vec{q}

Here we discuss event-selection cuts which will be applied to ensure that the systematic errors due to acceptance losses remain very small.

For quasi-elastic events, the \vec{q} -vector can be reconstructed based on the scattered-electron momentum and direction measured by BigBite. A fiducial cut can be placed on the direction of \vec{q} to choose the central direction of the scattered nucleons. While Fermi motion will widen the image, the ideal case of elastic scattering can be used to map the acceptance to a position distribution of neutrons on HCal (and a similar proton distribution, taking into account the deflection by the dipole magnet). Potential systematic errors are greatly reduced by *using the same fiducial region for both neutron-coincident and proton-coincident measurements*. The ‘image’ of the fiducial region projected onto HCal will differ for protons and neutrons because of the vertical kick given to the protons by the dipole magnet. To first order, the effect of this offset can be prevented from introducing a difference in acceptance by using a reduced fiducial region. To determine whether a particular (θ, ϕ) point is within the fiducial, the direction and magnitude of the corresponding \vec{q} for elastic scattering are determined. The expected trajectories are then evaluated for *both* a neutron and a proton with that momentum. Only if both such particles would fall in the active region of HCal is the angular point within the fiducial.

As a result of the fiducial cut, the neutron image for the accepted elastic events would leave an empty strip at the top of the HCal acceptance. The size of this strip is determined by the shift in the proton image relative to the neutron image. Similarly the elastic protons occupy the top of HCal acceptance, leaving an unoccupied strip at the bottom of acceptance. The size of the strip follows from the vertical kick given to the protons by the dipole, the nucleon momentum, p_N , and the distance, L from the target to HCal. While quasi-elastic protons (and neutrons) are not guaranteed to remain within the acceptance, the matching of the acceptance losses is improved by this reduced fiducial cut.

It is prudent to reduce the acceptance corrections where practical. This can be effected by choosing a new smaller fiducial, based on BigBite measurements, by demanding that the \vec{q} vector point towards a further-reduced portion of the HCal face. A margin of safety, d , is excluded at the top and bottom edges. This defines a smaller ‘active’ area of HCal to be used in defining the fiducial cut. If d is chosen as $d = \frac{\delta}{p_N} L$ then, to first order, quasi-elastic coincidences with the electron within the fiducial cut will be lost only if the struck nucleon had a component of momentum of at least δ directed towards the edge of HCal. In addition, to match neutron and proton acceptances, events are rejected if *either* a neutron or a proton with the corresponding \vec{q} would pass near the top or bottom of HCal, within a distance corresponding to $\delta = 100$ MeV/c. The cost of applying this tighter fiducial cut is a smaller fractional acceptance for quasi-elastically scattered electrons. The rate calculations in this proposal include this cut. With these cuts, the estimated loss of acceptance due to Fermi motion will be less than 2% at both kinematic points. This limits the potential for systematic errors due to the difference in the loss of protons compared to neutrons. The cost of these cuts is a reduction by $\approx 15\%$ in the counting rate at the lower Q^2 point and a negligible loss at the higher. The loss of acceptance is justified by the decreased sensitivity to systematic error.

These considerations are illustrated graphically in Fig. 12. The blue shapes show the edges of the neutron (left) and proton (right) distributions which would be expected, for ideal elastic scattering, on the face of HCal for electrons which fall in the BigBite acceptance. The simulated quasielastic events within the BigBite acceptance are concentrated in this ‘elastic image’ but scatter

outside of it because of Fermi-motion of the struck nucleon. For protons, the elastic image actually goes beyond the top of HCal. Without a fiducial cut, this would lead to a different acceptance loss for protons than for neutrons. In fact, the fiducial cut (on \vec{q} , as reconstructed from BigBite alone) eliminates the part of the elastic image which would fall near the top of HCal. This causes the sharp horizontal cut in the quasielastic distribution below the top of HCal. For only a few events are the quasi-elastic protons scattered to the edge of the HCal acceptance. Since the *identical* fiducial cut is applied to all events, the neutron image also shows the same abrupt cutoff in density near the top of the elastic image. The solid angles are matched for the two nucleon species and the acceptance losses are almost identical. Fig. 13 shows a similar plot for the higher Q^2 point. Here, the kinematics make the BigBite image on HCal much more compact and the fiducial cut has no impact.

7 Nucleon Detection Efficiency

While the efficiency of electron-detection cancels in the ratio, R'' (equation 1), that is not true for the neutron or proton detection efficiencies. The efficiency of HCal's detection of these particles must be well matched and/or well understood to control systematic errors. As shown in Figs. 9 and 10, the efficiency is very high and quite constant for neutron momenta corresponding to the kinematics of interest. At significantly lower momenta, it falls off simply because a high threshold has been chosen for running at these kinematics.

Fortunately the efficiency may be expected to be quite stable since it is largely determined by the mass distribution in the detector and the resulting probability of hadronic shower initiation. Factors, such as gain, threshold, and light yield have a relatively minor effect since most showers produce large numbers of secondaries and so their total light output is well above threshold. This stability is demonstrated in Fig. 14 which shows the *ratio* of the efficiency found [51] for a threshold of 2.4 GeV to that found with a threshold of 2.1 GeV. A 15% change in threshold (or gain) is seen to have nearly negligible effect on the efficiency at the two highest momentum points, which correspond to the center of the quasielastic peaks at the two kinematic points of this proposal. This is in contrast to detection of low energy neutrons in scintillator, for which the detection efficiency is a strong function of effective threshold. Furthermore, since HCal's detection is based purely on scintillation, it is immune to the rapid changes in efficiency and background which can more typically occur in wire chambers. Furthermore, as can be seen from the lower-momentum points, the falloff in efficiency is almost identical for neutrons and proton, meaning that it would largely cancel in the ratio, R'' (equation 1).

Neutron efficiency measurements at lower nucleon momenta are planned as part of E-09-019, which would run contiguously with the proposed experiment. These high Q^2 points will benefit from that calibration and the lower Q^2 measurements, themselves, to use high-statistics data to probe the uniformity of response of the calorimeter modules. Proton efficiencies are relatively easy to measure, using liquid Hydrogen as a source of tagged protons. These measurements will be made at the kinematics of the present experiment (over part of the face of HCAL) and should serve as a rigorous test of the accuracy of simulations. Since the neutron efficiency is intrinsically close to the proton efficiency for such a detector, a measurement near the expected efficiency will imply that the detector is working as expected for both nucleons.

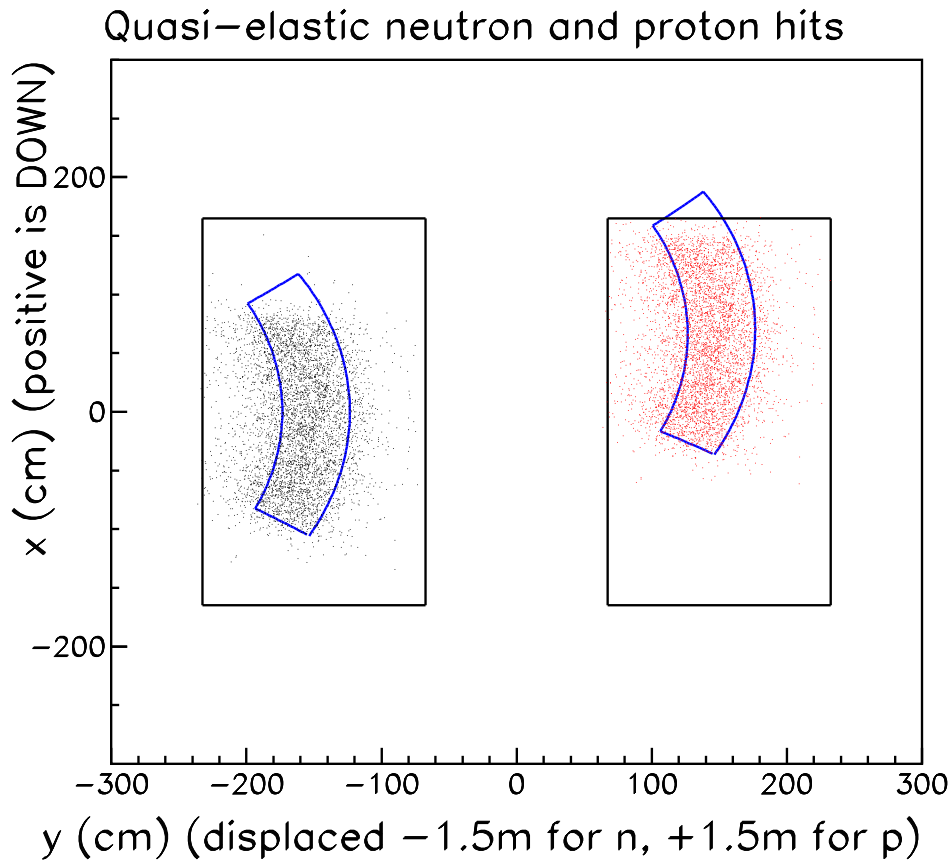


Figure 12: Effect of the fiducial cut for $Q^2=16$ (GeV/c)² kinematics is illustrated. The face of the HCal detector is shown (rectangle) with a superimposed blue outline of the region which would be covered by *elastically* scattered nucleons for which the corresponding electron falls within the acceptance of BigBite. For clarity the image for neutrons and protons are shown side-by-side rather than superimposed. Dots indicate positions of neutron (black) or proton (red) hits from simulated quasi-elastic events subject to the fiducial cut.

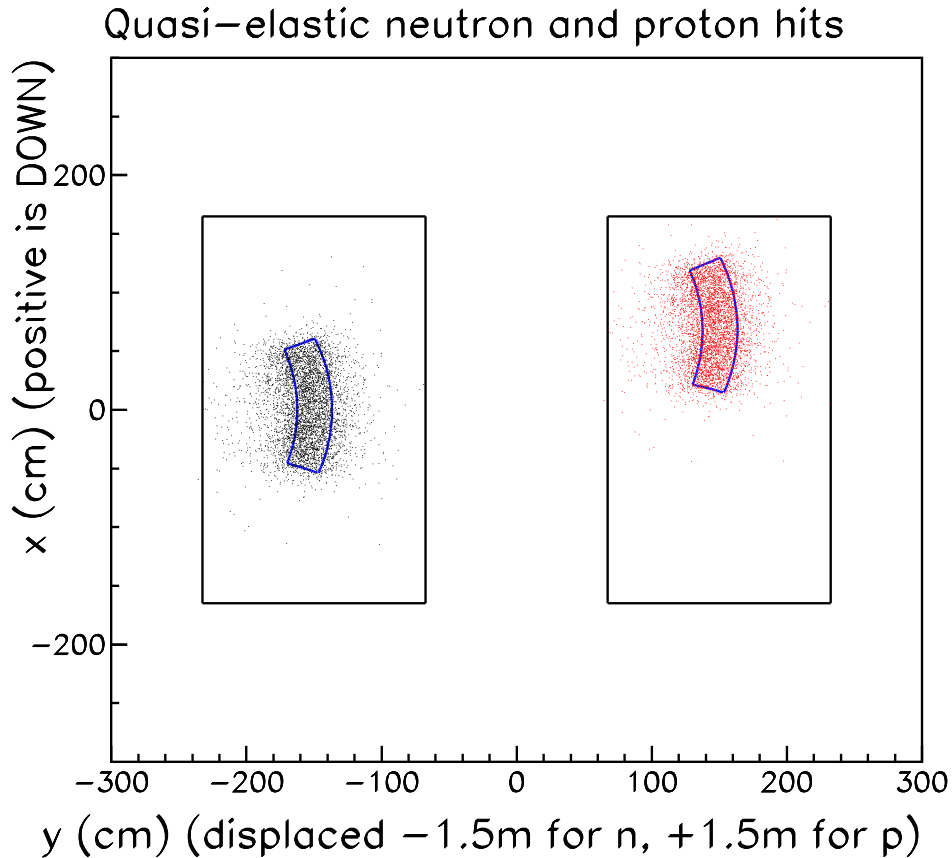


Figure 13: Effect of the fiducial cut for $Q^2=18$ (GeV/c)² kinematics is illustrated. The face of the HCal detector is shown (rectangle) with a superimposed blue outline of the region which would be covered by *elastically* scattered nucleons for which the corresponding electron falls within the acceptance of BigBite. For clarity the image for neutrons and protons are shown side-by-side rather than superimposed. Dots indicate positions of neutron (black) or proton (red) hits from simulated quasi-elastic events subject to the fiducial cut.

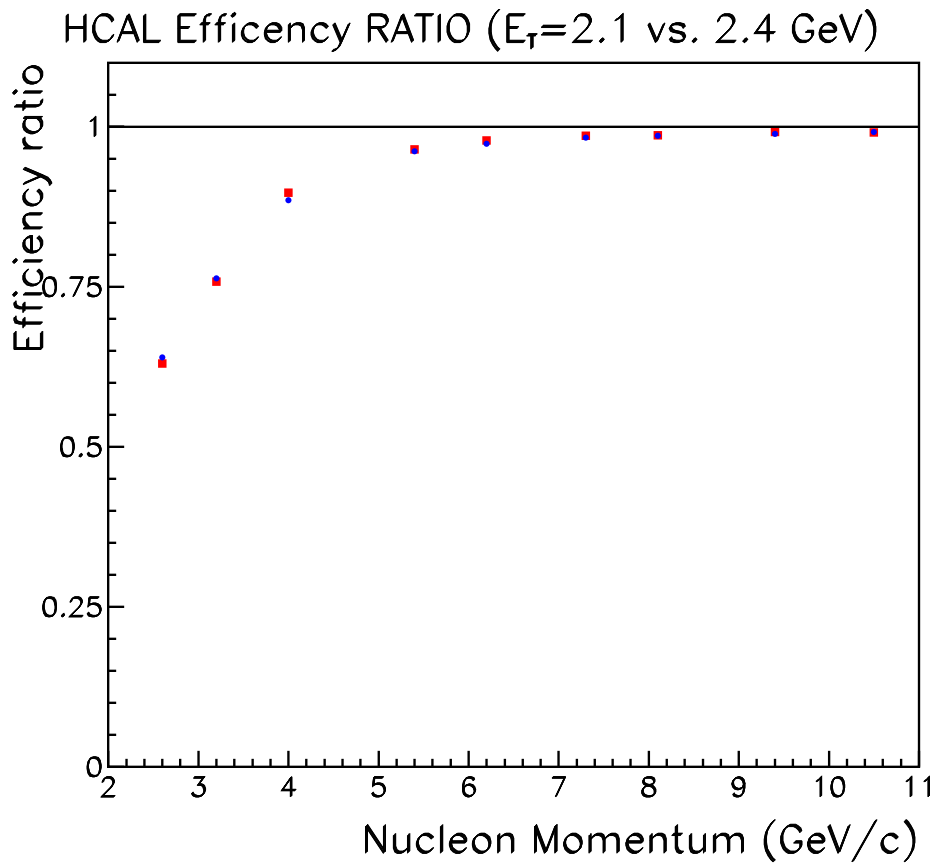


Figure 14: The predicted [51] *ratio* of the detection efficiency of HCal with a threshold of 2.1 GeV (planned for the lower Q^2 point) compared to a threshold of 2.4 GeV (planned for the higher Q^2 point) is shown for neutrons (blue circles) and protons (red squares) as a function of nucleon momentum. The momenta of interest for the present proposal are centered at the two highest points plotted.

8 Simulations

At high Q^2 the kinematic separation of quasi-elastic and inelastic events becomes more washed-out by the kinematic-broadening effects of Fermi motion in the deuteron. Also the size of the inelastic cross section relative to the quasi-elastic grows rapidly with increasing Q^2 . A simulation is needed to determine whether there is a serious problem with contamination of the quasi-elastic coincidence signal by inelastic events for which a nucleon hits the HCal near where a quasi-elastic nucleon would be expected.

This section will present the technical details of the implementation of the simulations, including the normalization of the inelastic spectrum relative to the quasi-elastic. The next section will present the results of the simulations.

8.1 Quasi-elastic

Simulation of the quasi-elastic signal was carried out in a spectator model in which the virtual photon was assumed to interact with only one nucleon while the other simply escaped. This implies that the spectator nucleon is projected into ‘on-shell’ kinematics by the interaction (with whatever initial momentum it has) and so the initial off-shell mass of the struck nucleon is determined by the requirements of energy conservation. While off-shell effects were included at the kinematic level, no attempt was made to modify the electron-nucleon scattering cross section to reflect the off-shell nature of the struck nucleon.

In the previous proposal (E-09-019) the scaled dipole form factors were assumed for the nucleons in making rate estimates (except the Galster parameterization was used for the neutron electric form factor). This was chosen to allow direct comparison of the proposal with a CLAS12 experiment (E12-07-104) [54] which used the same parameterization and covered an overlapping Q^2 range. The dipole approximation is known to fail for the proton electric form factor [2, 3] and the highest Q^2 SLAC measurements [26] of G_M^n indicate that it falls off significantly more rapidly with Q^2 than does the dipole. In view of this it is more conservative to use a more modern parameterization of the form factors [38], especially at such high Q^2 . This parameterization for G_M^n is shown in Fig. 1. Similar parameterizations for the other form factors are also given by the same authors. They are based on parameterization of Kelly [55] but have been constrained to satisfy quark-hadron duality constraints at high Q^2 . This parameterization was used in the present proposal for all rate estimates and to normalize estimates of inelastic background.

As described below, kinematic effects of the initial motion of the nucleon were reflected by calculating the cross section based on the electron energy and scattering angle as determined in the rest frame of the scattered nucleon.

The momentum distribution of nucleons was taken from the momentum-space wave-function (non-relativistic Fourier transform of spatial wave-function) for a Lomon and Feshbach deuteron potential. The particular model used (#10 from reference [56]) gave 5.79% D-state and included a hard core. The hard core is reflected in a high-momentum tail in the momentum-space wave-function making this a somewhat ‘worst case’ simulation.

In brief, the steps of each quasi-elastic event simulation are summarized here. A Fermi momentum was chosen for the struck nucleon based on the probability distribution for magnitude of p derived from the deuteron wave-function. A direction was chosen isotropically. The corresponding kinetic energy of the on-shell spectator was subtracted from the deuteron mass to find the

kinematically-consistent initial energy of the struck nucleon from which the (off-shell) invariant mass of the struck nucleon was found. The beam electron was then rotated and boosted to a frame in which the nucleon was at rest (and the electron was rotated back onto the z-axis). A scattering angle was then chosen isotropically (flat in ϕ and in $\cos\theta$) and the elastic scattering cross section was evaluated for these rest-frame initial kinematics. The scattered energy was calculated with the added requirement that the off-shell initial-state nucleon be promoted to an on-shell nucleon in the final state. Some 'sanity cuts' were applied to eliminate extreme cases in which the quasi-elastic model was clearly pushed beyond the range of applicability, such as cases with off-shell invariant mass of the struck nucleon being less than 10% of the nucleon mass or final electron energy being unphysical. All boosts and rotations were then inverted on the final-state particles to return them to the lab frame. No kinematic weighting was done on the distributions of Fermi momentum or scattering angle to reflect the greater probability of scattering at small angles and at kinematics which lead to lower electron energy in the nucleon rest frame. The higher weighting of these events was reflected in the calculated cross section, which was then used to weight the entries made to the final-state distributions. Thus the simulation not only properly accounted for these kinematic effects, it also resulted in properly normalized cross sections for the simulated reaction. To select the quasi-elastic events of interest, an acceptance cut was imposed to require that the electron fell into the BigBite acceptance while the scattered nucleon fell into the HCal acceptance. The effects of finite-resolution were then incorporated by smearing the final electron-energy angle and energy by Gaussian distributions to simulate the BigBite resolution and similarly smearing the detected nucleon angle to reflect the HCal resolution. The resulting quantities were then used to calculate W^2 and θ_{pq} and the simulated distributions of the quantities of interest were incremented, weighted by cross section. Here θ_{pq} , introduced above, is the angle between the calculated \vec{q} direction and the observed scattered nucleon direction while W^2 is the squared missing-mass of the hadronic system as calculated assuming a stationary proton target (i.e. $W^2 = (m_p + \omega)^2 - (\vec{q})^2 = m_p^2 + 2m_p\omega - Q^2$).

8.2 Inelastic

The term "inelastic" is used here to imply particle production and is exclusive of quasi-elastic events. Simulation of inelastic events required a more sophisticated model for the basic interaction on the nucleon. This was done with the use of the Genev physics Monte-Carlo [59] written by the Genoa group and used extensively in simulations for CLAS. This program is designed to simulate with, reasonable empirical distributions, production of multi-pion final states and production and decay of Delta's, rho mesons, and omega meson (phi meson production was not enabled when the simulations were run). It can simulate neutron or proton targets and both were used in simulating inelastic events from the deuteron.

The smearing effects of Fermi motion for quasi-free inelastic production from the nucleons in the deuteron were included in a similar way to that described above for the quasi-elastic production. There was, however, no mechanism to put the initial-state nucleon off-shell for the initial state used by Genev. The spectator model was therefore implemented by treating the initial state as two on-shell nucleons with equal and opposite Fermi-momentum (in the deuteron rest frame). The effective violation of conservation of energy implied by this approximation is modest (a few tens of MeV) and is expected to have the effect of widening tails and so causing backgrounds to be over-estimated if anything.

Final-state distributions were simulated separately for electro-production off the neutron and

proton. The same momentum-state wave-function was used to generate the initial momentum distribution of the target nucleons. After rotating and boosting to the nucleon rest frame the energy of the incident electron was passed to a Genev-based subroutine which simulated a single inelastic event for the chosen effective beam energy. The scattered electron direction was selected randomly (both θ and azimuthal angle, ϕ) by Genev based on cross-section-weighting subject to constraints on W^2 and Q^2 , discussed below. The predicted final-state particles were then boosted and rotated back to the lab frame by reversing all boosts and rotations done to the initial-state particles. In order to make effective use of simulated events without biasing distributions, those events which had a final electron azimuthal angle outside the range of -20° to $+20^\circ$ were rotated about the beam direction by an angle chosen to give a final azimuthal angle chosen randomly within that range. This enhanced the yield of events within the BigBite acceptance but didn't affect distributions which had, at minimum, a requirement of a hit in BigBite.

The range of Q^2 and W^2 to be generated by Genev was selected empirically since the effects of Fermi motion made it difficult to predict the significant range *a priori*. A low-statistics run of the simulation with a broad range was subjected to the acceptance cut of BigBite for the angle(s) of interest for the beam energy being simulated. The resulting Q^2 and W^2 distribution showed clear peaks in the regions which were relevant for scattering into BigBite. High statistics runs were then done with those ranges selected for generation of Genev events.

Full kinematic information was written out for each event (including particle identification for each four-vector). These were then selected to produce samples of interest for each kinematic point which would have an electron within the BigBite acceptance. The effects of finite detector resolution were folded in (by smearing of each four-vector) before calculation of kinematic quantities of interest such as W^2 and θ_{pq} .

8.3 Inelastic Background Normalization

A fundamental difference between the quasi-elastic and inelastic simulations is that the inelastic simulation produced simulated events without a corresponding cross section by which to weight them. While the relative cross sections were accounted for in the probability of generation of different types and topologies of events, an overall normalization is needed to allow comparison of the inelastic events (from each target nucleon) with the quasi-elastic results.

Normalization of inelastic to quasi-elastic cross sections was done empirically, using SLAC spectra for single-arm electron scattering from the deuteron. Figure 15 shows spectra from [60] and [26] used for the normalization. The kinematic coverage of those measurements (truncated to the W^2 range of relevance) is shown in Fig. 16 with the same colors as in Fig. 15 to distinguish the two data sets. Two conveniently chosen ranges were used to characterize the cross sections in the quasi-elastic and inelastic regions. These are shown in Fig. 15 as green bars indicating the limits selected for the ‘‘Quasi-elastic region’’ ($0.5 < W^2 < 0.88 \text{ GeV}^2$) and red bars indicating the limits selected to define the ‘‘Inelastic region’’ ($1.3 < W^2 < 1.7 \text{ GeV}^2$). As can be seen from the figures, the regions were chosen to give samples which were almost purely representative of the indicated final state, without significant contamination of inelastic events in the Quasi-elastic region or *vice versa*. The Inelastic region was also chosen close to the quasi-elastic peak so it would be representative of the events which would be likely to cause background.

Within the quasi-elastic model, the kinematic variation of cross-section within the Quasi-elastic region would be expected to follow the sum of the elastic cross sections for scattering from the proton

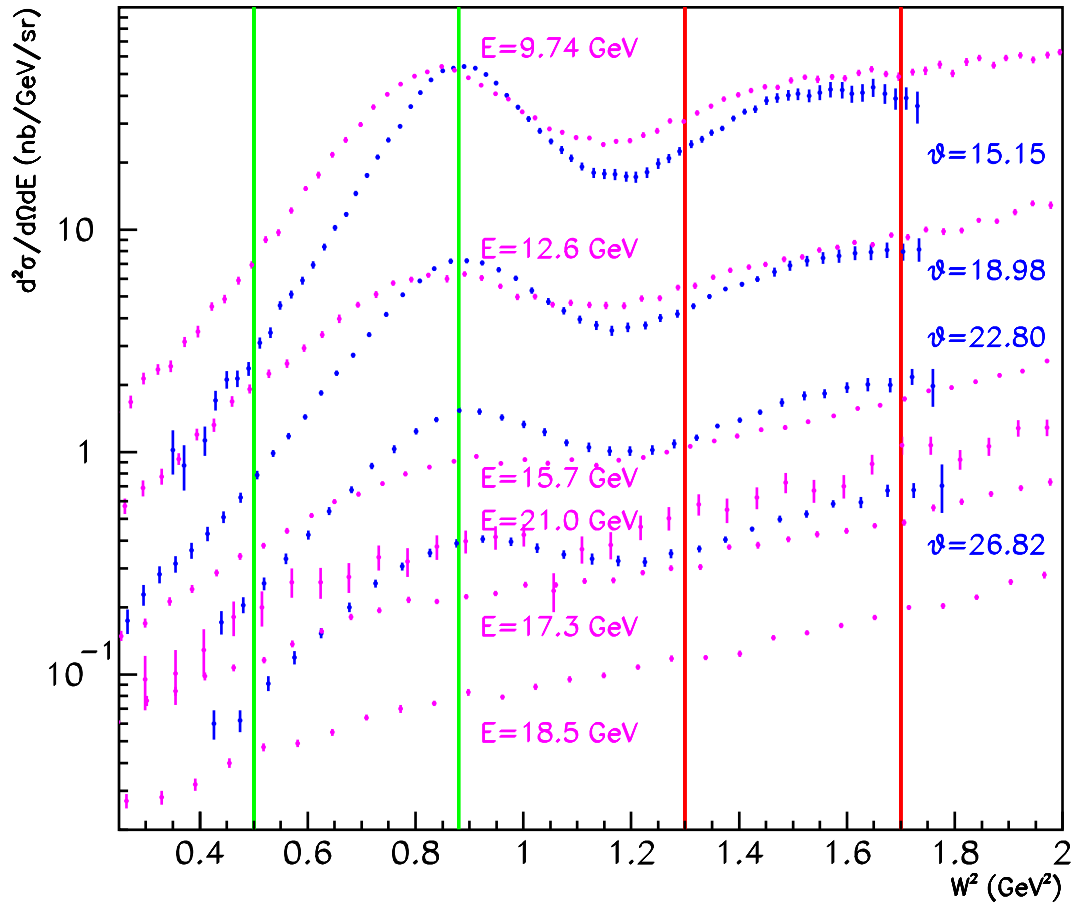


Figure 15: Measured single-arm spectra from SLAC covering the quasi-elastic and inelastic regions. Blue points were taken at $E=5.507$ GeV and indicated angle (in degrees). Magenta points were taken at indicated energy and $\theta = 10^\circ$.

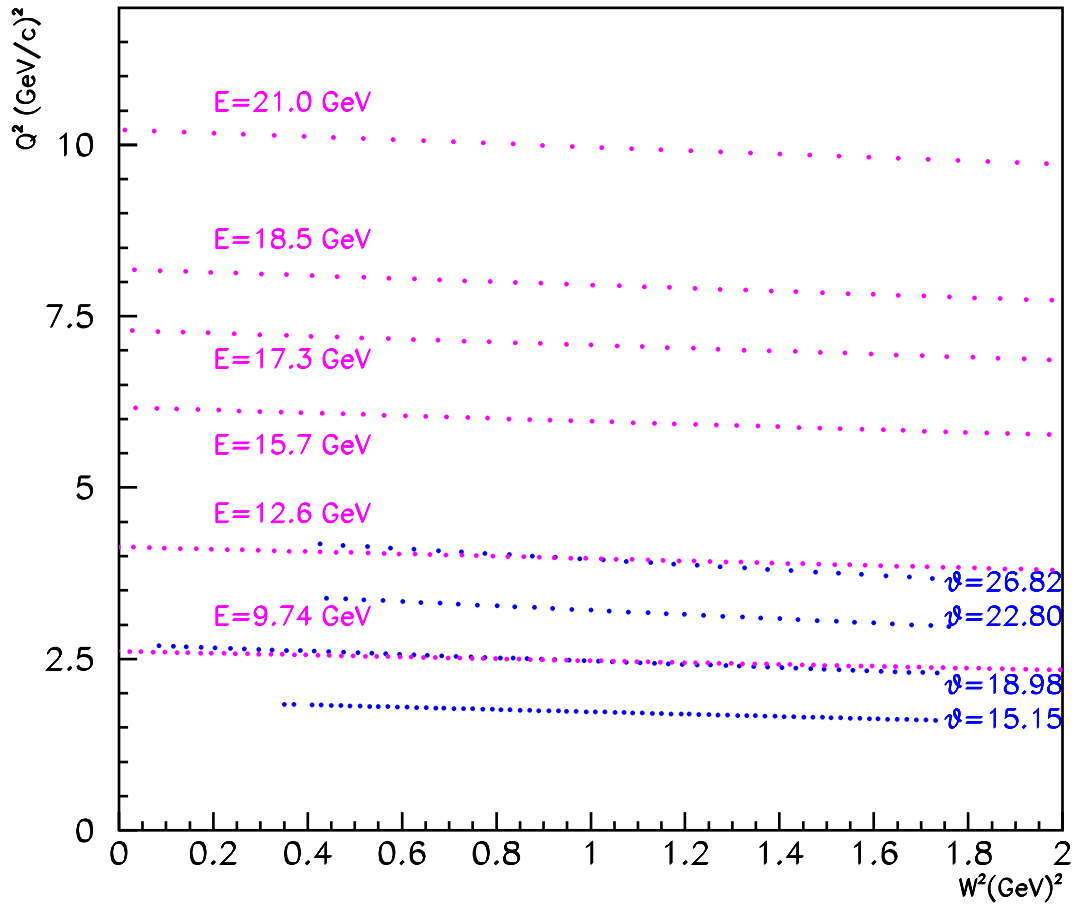


Figure 16: The Q^2 vs. W^2 coverage corresponding to the spectra of the previous figure.

and neutron. The numerically summed cross section in the Quasi-elastic region of each spectrum was divided by the predicted sum of proton-elastic and neutron-elastic (based on scaled-dipole and Galster) to obtain a measured strength (which was quite stable at a value of ≈ 0.35). Similarly, based on

$$\frac{d^2\sigma}{d\Omega dE'} = \frac{\alpha E'(W^2 - m_p^2)/(2m_p)}{4\pi^2 Q^2 E} \frac{2}{1 - \epsilon} (\sigma_T(W^2, Q^2) + \epsilon\sigma_L(W^2, Q^2))$$

the kinematic factors were divided out of each bin of the double-differential cross section in the Inelastic region to yield the corresponding value of $(\sigma_T + \epsilon\sigma_L)$. Since the non-resonant background dominates over Δ production in these spectra, a non-resonant empirical scaling of $\sigma_L/\sigma_T \approx 0.25/\sqrt{Q^2}$ was used to allow σ_T (summed over the Inelastic region) to be extracted for each spectrum. (An alternate extreme would be to treat the inelastic cross section as purely transverse, as it might be if the Δ dominated. This was tried and resulted in only a modest change in the predicted inelastic strength at the kinematics of interest.) The inelastic/quasi elastic strength can then be characterized as the ratio of the extracted σ_T from the Inelastic region divided by the scaled cross-section from the Quasi-elastic region. This ratio (for both sets of SLAC kinematics) was found to be reasonably well parameterized as a simple parabolic function of Q^2 ($r = 0.015 \frac{Q^2}{(\text{GeV}/c)^2}$). This form was then used to predict the inelastic cross section within the Inelastic region for the Q^2 applicable for the beam energy and scattering angle of the kinematics of interest. These were found as multiples of the summed simulated cross section in the Quasi-elastic region (divided by the sum of proton and neutron elastic cross sections).

This gave the total normalization of the inelastic cross section. It remained to find individual scaling factors for the proton-target and neutron-target inelastic cross section to simulate the deuteron cross section. The inelastic cross section on the neutron was taken to be half of the inelastic cross section on the proton. Since the final state distributions (including individual measure of proton-coincidences or neutron-coincidences) were almost identical for the two assumed targets, the final results are almost insensitive to this choice of relative strength. This then allowed scaling factors to be determined to scale the number of simulated events to a double-differential cross section. These normalized results are shown in the next section.

9 Inelastic Background

Results from the simulations of inelastic contributions are shown in Figures 17 and 18 for the kinematic of interest. Each figure represents one of the kinematics shown in Table 1.

In all simulated spectra, the statistical fluctuations reflect the statistics of the Monte-Carlo simulations and are not intended to simulate the statistics acquired by the proposed experiment.

The plots on the left in each figure show the neutron-coincident quasi-elastic (red) and inelastic (blue) spectra and their sum (black), integrated over the acceptance of the experiment. The plots on the right show the equivalent proton-coincident spectra. Proton- and neutron- coincidence here, as in the proposed experiment, are defined based on proximity of the simulated HCal hit to the position which would be predicted based on the \vec{q} -vector constructed based on the resolution-smearred information from BigBite.

The upper plots show the W^2 spectra. Kinematic broadening and the large inelastic cross sections are seen to result in a large contribution of inelastic events under the quasi-elastic peak.

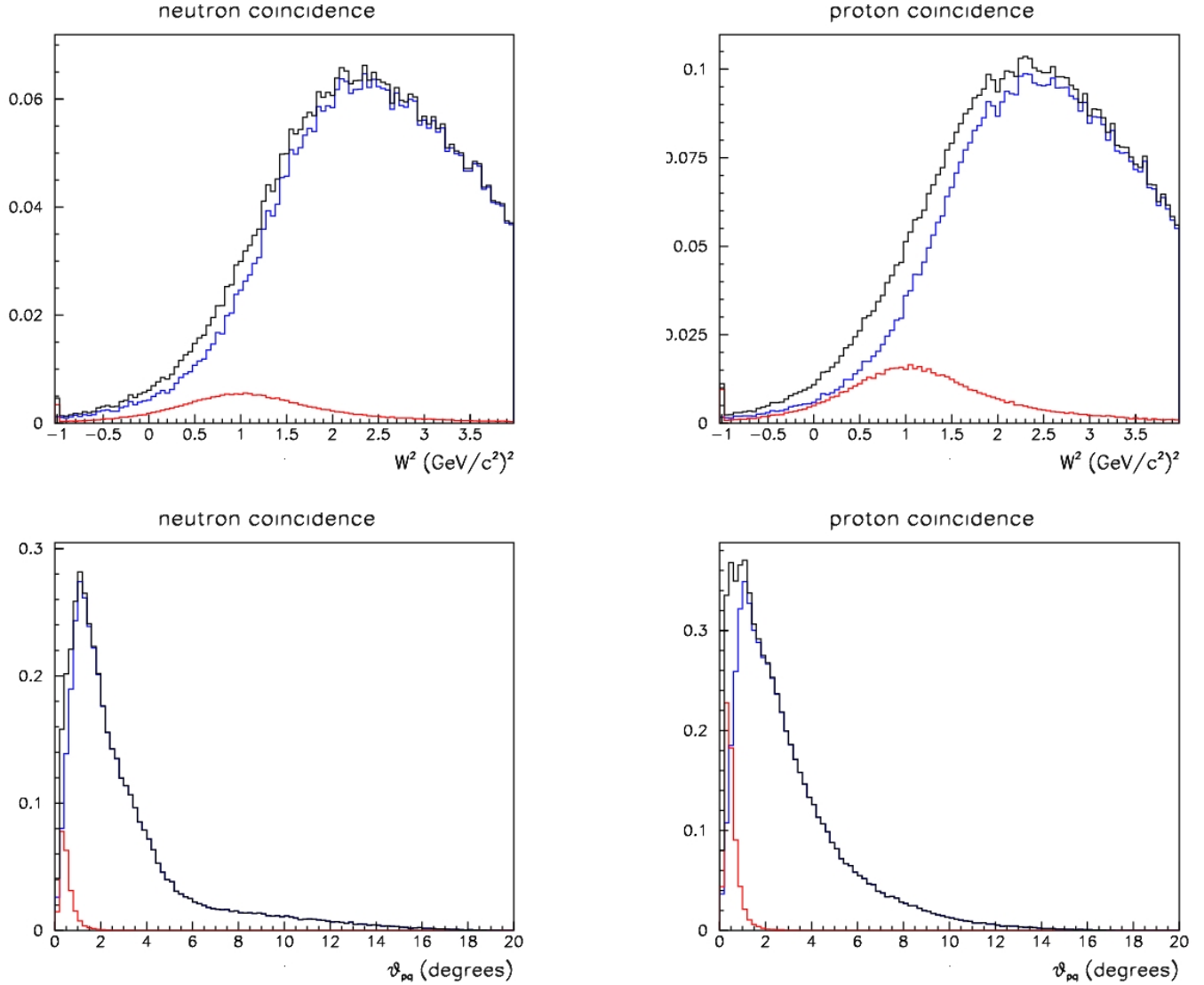


Figure 17: Projections onto W^2 and θ_{pq} for simulations of inelastic background (blue) and quasi-elastic (red) cross section for the $Q^2 = 16$ (GeV/c)² kinematic point. Vertical axes are efficiency- and acceptance-weighted cross section integrated over the combined spectrometer acceptance, in fb/bin.

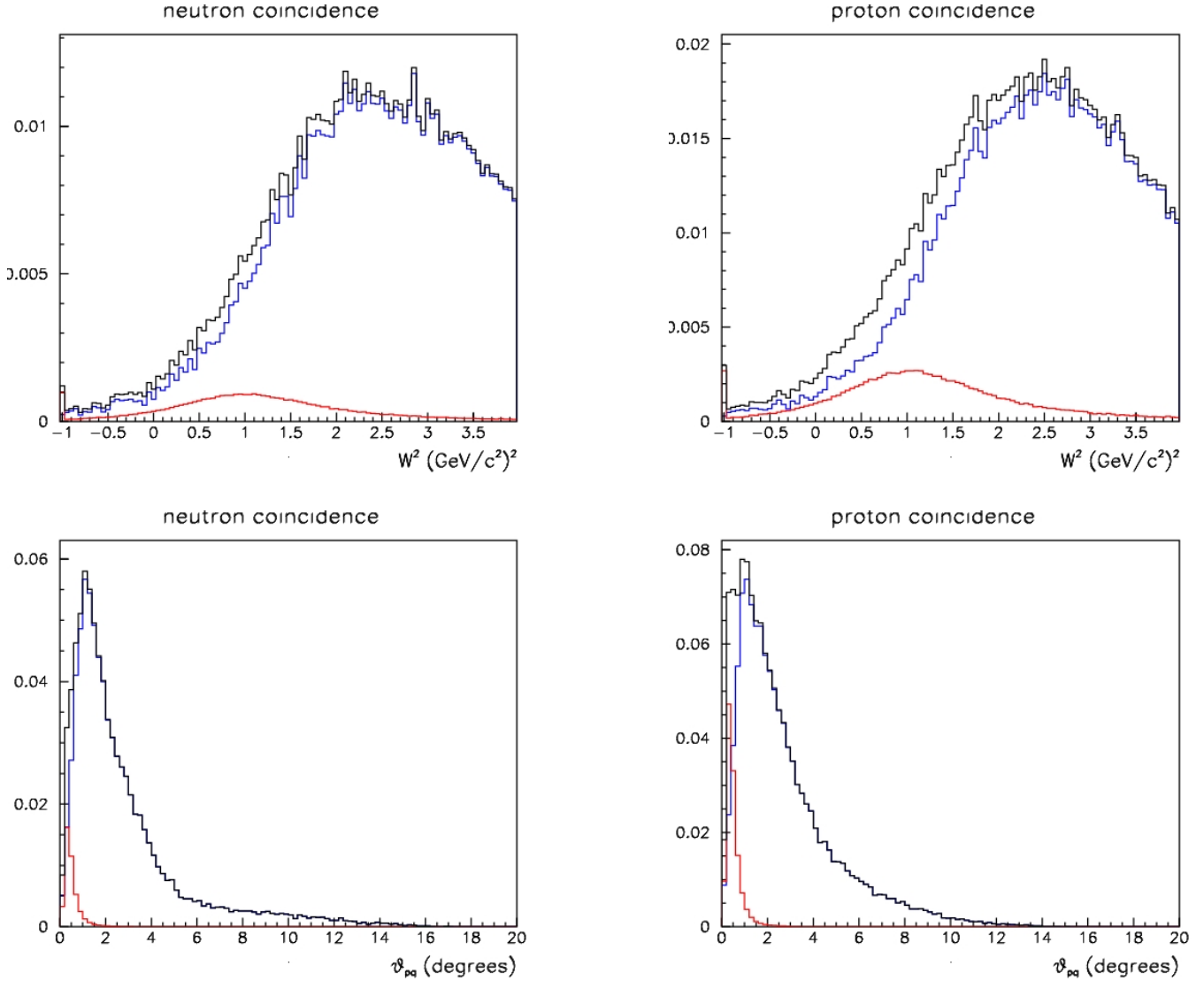


Figure 18: Projections onto W^2 and θ_{pq} for simulations of inelastic background (blue) and quasi-elastic (red) cross section for the $Q^2 = 18$ (GeV/c)² kinematic point. Vertical axes are efficiency- and acceptance-weighted cross section integrated over the combined spectrometer acceptance, in fb/bin.

Without additional cuts to reduce this contamination, this would present a very significant problem for these measurements.

The lower plots show the distributions of θ_{pq} . As mentioned above, θ_{pq} is the angle between direction of the nucleon's momentum (\vec{p}), reconstructed from the position of the hit on HCal, and the momentum-transfer vector (\vec{q}), as reconstructed based on the scattered-electron's energy and direction. For elastic scattering from a nucleon at rest, θ_{pq} would peak sharply at zero, having a finite width only due to measurement resolution. For quasi-elastic scattering, θ_{pq} is broadened by the unknown initial momentum of the struck nucleon. However, it is seen to still be sharply peaked. Simulations done for E-09-019 showed that, as expected, the θ_{pq} distribution becomes more sharply peaked with increasing Q^2 . At the $Q^2 = 16$ and 18 (GeV/c)² points shown in Figs. 17 and 18, the quasi-elastic θ_{pq} distribution is very narrow, being almost entirely below $\theta_{pq} = 1^\circ$. The distribution for inelastic events is seen to be much wider. This provides a very important additional cut which can be used to select the quasi-elastic events of interest and reject the background from inelastic events. Here the excellent angular resolution of HCal, due to its good transverse spatial resolution and 17 meter lever-arm, becomes an important asset. Furthermore, the linear rise of the inelastic distribution (which is a geometric effect, reflecting a roughly constant density of nucleon hits per unit area in the region pointed to by the \vec{q} vector) suggests the possibility of correcting for residual inelastic contamination by extrapolating the large-angle θ_{pq} spectrum into the region of the cut and predicting the contribution of inelastic events surviving the cut.

From the figures presented above, it is clear that the inelastic background is largest in the case of neutron-coincident measurements. Figs. 19 and 20 present additional results from the simulation for neutron-coincident spectra, demonstrating the effect of cuts on θ_{pq} . The signal-to-noise ratio is seen to improve as the cut is tightened. For a cut tighter than $\theta_{pq} < 1^\circ$ the accepted quasi-elastic coincidence cross section is seen to decrease (as expected from the θ_{pq} plot shown in Figs. 17 and 18).

The optimal choice of cuts on W^2 and θ_{pq} involves a trade-off of statistics against signal purity. Integration of the $Q^2 = 18$ (GeV/c)² spectra for the $\theta_{pq} < .5^\circ$ cut, for example, indicates that the inelastic background can be reduced to less than 21% contamination by applying a very tight cut selecting $-0.95 < W^2 < 0.5$ GeV² at a cost of 79% of the quasi-elastic acceptance. The accepted signal could be more than doubled by increasing the upper W^2 cut-off to 1.0 GeV² while only increasing the background to 22%. Similarly increasing the cut-off to 1.5 GeV² would add another 50% to the integrated signal but would increase the background contamination to 27%. (We refer to background contamination as background/total.)

The best cuts will have to be chosen based on the observed data, estimated background contamination and estimated systematic error on the determination of the background. For the simulated data presented here, a set of cuts was chosen to minimize the error on the extracted value of R. These were based on the simulated spectra, the anticipated luminosity and running time requested in the present proposal, and an assumed 20% systematic error (in addition to \sqrt{n} statistical error) on the background contamination. The fractional systematic error was assumed to be common in the neutron and proton contamination and so partly canceled in the evaluation of R. For the actual analysis, a locus in $W^2 - \theta_{pq}$ space might be used to select events. For the purpose of rate estimates, a simple rectangular region was selected by optimizing separate cuts on W^2 and θ_{pq} .

The resulting optimal cuts and anticipated contamination are presented in Table 3. These results are used below in estimation of systematic errors. The contamination fractions listed in Table 3 are the values before correction. Given a 20% systematic error, the majority of the contamination would

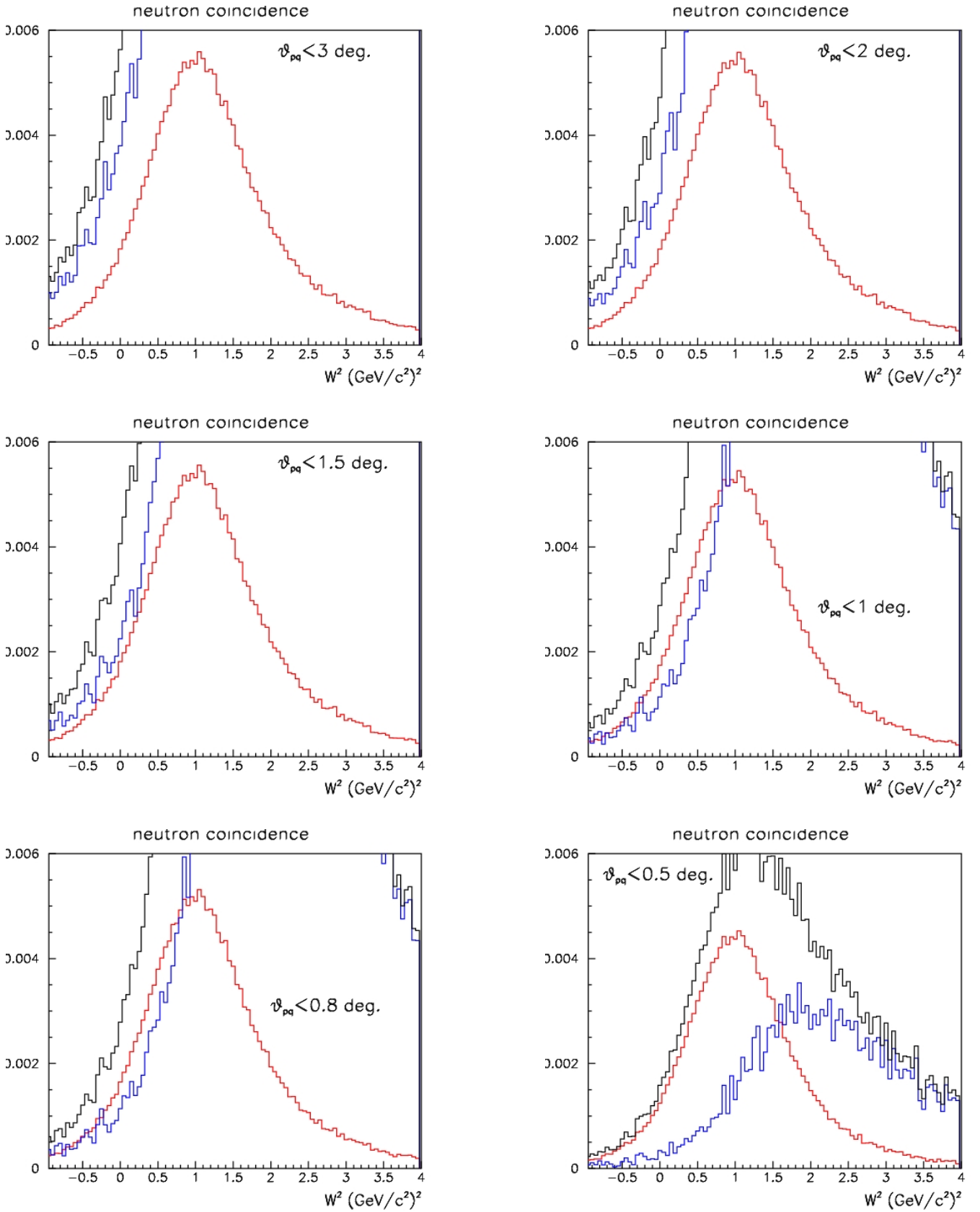


Figure 19: Quasi-elastic (red) and inelastic (blue) cross-section vs. W^2 with coincident neutron detection with different cuts on θ_{pq} for the $Q^2 = 16$ $(\text{GeV}/c^2)^2$ kinematic point. The cuts applied to θ_{pq} are indicated on each plot. The vertical axis for each plot is the efficiency- and acceptance-weighted integrated cross section in fb/bin.

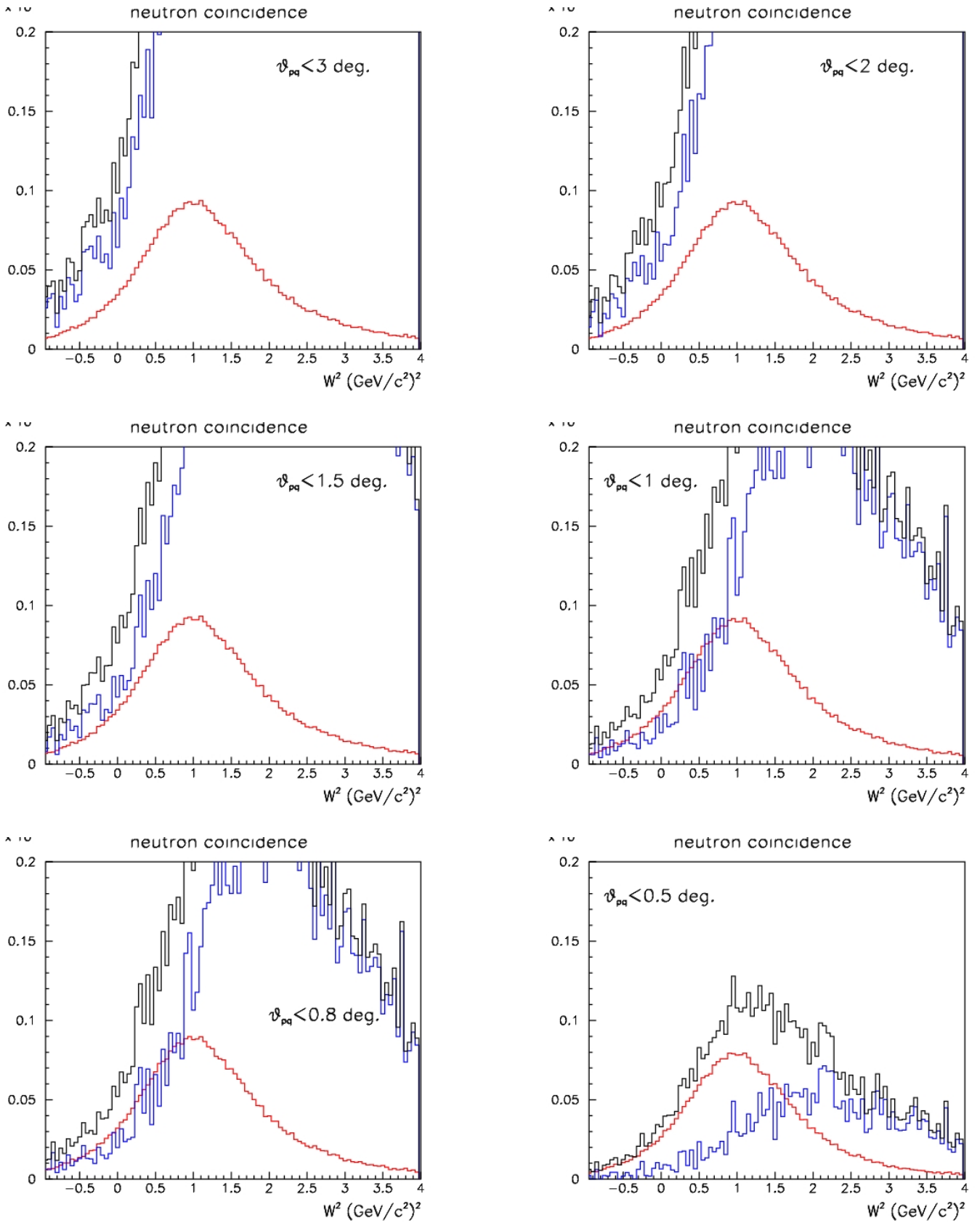


Figure 20: Quasi-elastic (red) and inelastic (blue) cross-section vs. W^2 with coincident neutron detection with different cuts on θ_{pq} for the $Q^2 = 18$ $(\text{GeV}/c)^2$ kinematic point. The cuts applied to θ_{pq} are indicated on each plot. The vertical axis for each plot is the efficiency- and acceptance-weighted integrated cross section in fb/bin.

Table 3: Estimated fractional contamination of inelastic events in the quasi-elastic sample after W^2 and θ_{pq} cuts but *before any correction is applied*

Q^2 (GeV/c) ²	16.	18.
Max. θ_{pq} (deg.)	0.5	0.5
Max. W^2 (GeV ²)	1.6	2.0
Proton contamination (%)	14	20
Neutron contamination (%)	28	34

be subtracted off. Since the inelastic backgrounds in the neutron and proton spectra are expected to be of similar shape (and will be extrapolated into the quasi-elastic region using similar shapes) if one background is underestimated the other may also be expected to be underestimated. Similarly, if the neutron background is oversubtracted, the proton background will also be oversubtracted. As mentioned above, this common error in the numerator and denominator partly cancels in evaluation of the ratio, R'' . The cancellation is not complete because the fractional errors in the numerator and denominator will differ. But the partial cancellation results in a fractional error on the ratio, due to systematic background error, which is smaller than the fractional error contributed to the neutron or proton counts.

10 Rates and Trigger

In this section we review the inputs used in the rate calculations and give the expected rates for the quasi-elastic coincidence measurements and for the calibration reactions.

Since background rates are roughly proportional to the number of target nucleons, rate estimates are based on a luminosity of $\mathcal{L} = 2.8 \times 10^{38}/A \text{ cm}^{-2}\text{s}^{-1}$, where A is the number of nucleons in the target. While this exceeds our experience in the GEN experiment [44] using similar apparatus, there are several factors which decrease the susceptibility of the present experiment to accidental background. The observed rate of accidental events above threshold in BigHAND was ≈ 2 MHz for that measurement. HCal will be significantly further back from the target (17 m compared to 6.5 to 12 m for GEN running) so a much smaller solid angle is subtended. More importantly, HCal will be virtually immune to low energy background, running with a trigger which requires ≈ 40 MeV (electron equivalent) deposited in the scintillator, corresponding to more than a GeV of total energy deposited. BigBite will be instrumented with GEM detectors which should be able to handle a significantly higher luminosity than proposed here.

A Monte Carlo [45] simulation has been done to predict the background BigBite trigger rates which will may be expected as a function of the threshold applied to the electromagnetic calorimeter. The simulation included a parameterization of expected light-generation by hadrons. Pion rates were based on an empirical fit to observed charged pion production rates measured at SLAC. A parameterization of electron-scattering rates from deep inelastic scattering was also included. The results of the simulations at the kinematic points of this experiment are shown in Fig. 21. For each kinematic point, the threshold must be chosen low enough so that quasielastic events are accepted with reasonable efficiency. An advantage of the ratio method is that there is no systematic error

Table 4: Suitable thresholds for the electromagnetic calorimeter trigger are listed. For comparison, the lower limit for quasi-elastically scattered electrons is also given.

Q^2	16.	18.
Quasi-elastic E'_{\min} (GeV)	2.1	1.2
Threshold (GeV)	1.9	1.0

introduced by such an inefficiency since it would be independent of the type of recoiling nucleon. Table 4 lists, for each kinematic point, the lower limit for scattered-electron energy for quasielastic events, as determined from the quasi-elastic Monte Carlo. The table also lists suitable threshold values which are $\approx 10\%$ below this minimum. Comparing those thresholds to Fig. 21 shows that the expected background trigger rates are comfortably low, being below 2 kHz even for the higher Q^2 point. Even a loose HCal coincidence requirement will then reduce the trigger rate to rates which are suitable even with the existing Hall A data acquisition system.

The threshold on the electromagnetic calorimeter will serve to reduce the trigger rate due to low energy scattered electrons from inelastic events. While suppression of inelastic events is generally advantageous, it is necessary to have a measure of the inelastic rate near the quasi-elastic peak in order to test and calibrate inelastic predictions which can then be used to correct for contamination under the quasielastic peak. Monte Carlo simulations of the effect of a threshold-cut on scattered electron energy have determined that these thresholds will cause negligible distortion of the inelastic background for $W^2 < 2.5$ (GeV/c) 2 .

For all rate calculations the track-reconstruction efficiency in BigBite was taken to be 75% and the trigger live time was taken to be 80%. The parameterizations of efficiencies for neutron and proton detection which were used are shown in Figs. 9 and 10. The actual values for the efficiencies, at the quasielastic peak, extracted from the simulation are given in Table 5.

The cross section for quasi-elastic scattering was numerically integrated over the combined acceptance of BigBite and HCal, subject to the fiducial cut, as described in section 8.1. The integrals, labeled as “ $\int \frac{d\sigma}{d\Omega} d\Omega$ ”, are given in Table 5. The line labeled “ W^2/θ_{pq} cut” gives the fraction of quasi-elastic events surviving the cuts, described in the previous section, used to reject inelastic events. Defining $\mathcal{L}_0 = 2.8 \times 10^{38}$ cm $^{-2}$ s $^{-1}$ = 1000/fb/hr, the luminosity for the quasi-elastic measurements on deuterium will be $\mathcal{L}_0/2 = 500$ /fb/hr. The resulting predicted rates of electron-nucleon coincidences are given in the first two lines of Table 6.

For proton efficiency measurements using elastic scattering on Hydrogen, the full combined solid angle of BigBite and HCal can be used, without a fiducial cut. For this calibration on an LH2 target, the full luminosity \mathcal{L}_0 can be used. The resulting rates are given in the third line of Table 6. high and will be estimated rather than based directly on calibration runs.

11 Systematic Errors

In this section we will estimate (or set upper limits on) contributions to the systematic error on the ratio R determined by this experiment. This helps set the scale for the statistical accuracy for which we should aim.

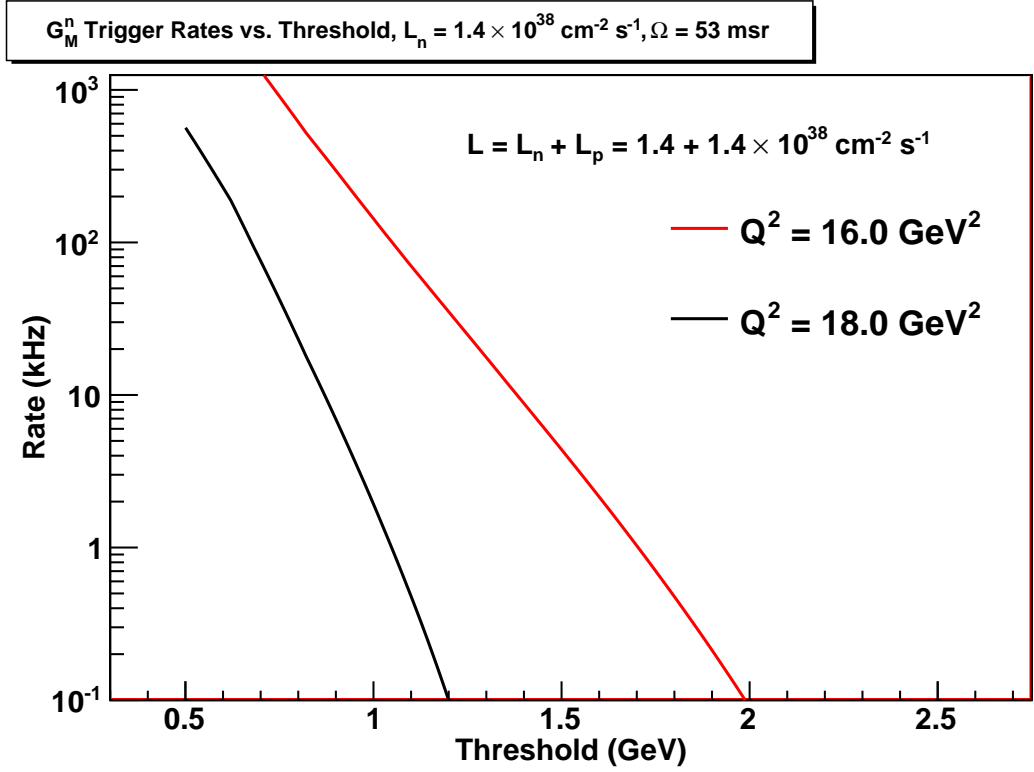


Figure 21: The predicted trigger rates from background particles as a function of the threshold applied to the electromagnetic calorimeter. Each curve represents one of the proposed kinematic points.

Table 5: Values used in calculating count rates.

$Q^2 \text{ (GeV/c)}^2$	16.	18.
θ_e	45.1°	65.2°
p efficiency (%)	96.8	96.5
n efficiency (%)	95.6	95.5
Quasi-elastic		
p-coinc. $\int \frac{d\sigma}{d\Omega} d\Omega$ (fb)	0.67	0.12
n-coinc. $\int \frac{d\sigma}{d\Omega} d\Omega$ (fb)	0.23	.044
W^2/θ_{pq} cut (%)	59	69

Table 6: Predicted Quasielastic coincidence rates (counts per hour)

Q^2 (GeV/c) ²	16.	18.
$d(e, e'p)$	108.	22.
$d(e, e'n)$	38.	7.9
$p(e, e'p)$	730	125

The use of the ratio method eliminates many potential sources of systematic error. Because $d(e, e'p)$ and $d(e, e'n)$ are measured simultaneously, their ratio is insensitive to target thickness, target density, beam current, beam structure, live time, trigger efficiency, electron track reconstruction efficiency, etc. So the fractional error achieved on the ratio can be much smaller than which could be achieved on the measurement of either cross section in itself.

Table 7 lists the estimated contributions to systematic errors, which are discussed in detail below.

The corrections needed to convert from the measured value R'' (Equation 1) to the quantity of interest, R (Equation 2) are only of the order of 1%, so systematic errors on them will be neglected.

The errors on the proton elastic cross section (needed to extract G_M^n from R) do not contribute to the error on the ratio G_M^n/G_M^p . This is a more fundamental result than G_M^n , itself, or the ratio of G_M^n to the scaled dipole. The ratio G_M^n/G_M^p is generally more directly calculable within a given theoretical model. While subsequent improvements in proton cross section measurements can be combined retrospectively with the R values from this experiment to improve the extraction of G_M^n , we include an estimated contribution to the error based on projected errors on G_M^p from an approved 12 GeV experiment [57]. We assume a 1.7% fractional error on the proton cross section at the lower Q^2 and 4% at the higher Q^2 , which is beyond the region to be covered in that measurement. This error should be included as a systematic in extraction of $(G_M^n)^2$, but not of the ratio G_M^n/G_M^p .

If G_E^n behaves like the Galster or Bodek [38] parameterizations at high Q^2 , then its contribution to the neutron cross section is small. Thus, even large fractional errors in G_E^n would produce only small errors in $(G_M^n)^2$. The contribution listed as G_E^n in Table 7 are based on an assumed error of 400% of the Galster parameterization.

Accidental coincidences of background events in HCal are not expected to cause significant systematic errors. Previous experience in the GEn experiment [44] showed a background rate of ≈ 2 MHz across the entire detector at a comparable luminosity (BigHAND saw about 12% the proposed luminosity, although BigBite viewed only a third of that). HCal will be significantly further from the target for this measurement and will have a much higher effective threshold so much lower rates may be expected. Even with a 1 MHz rate, the probability of an accidental coincidence within a 5 ns timing gate will be only 0.5% across the entire detector. The area searched for coincident protons or neutrons is limited by the $\theta_{pq} < 0.5^\circ$ cut to about 0.07 m² of the 5.4 m² face. So the rate of accidental coincidences is expected to be less than 0.01% for each nucleon species. Furthermore, this accidental contamination can be accurately estimated and subtracted by measuring the accidental coincidence rate in other parts of HCal, where true coincidences are not expected.

The target windows contain about 3.4% as many nucleons as the LD2 target. We use this as a conservative upper limit on the background contribution since very many of the events from aluminum will be rejected by the $\theta_{pq} < 0.5^\circ$ cut. This contribution will be subtracted off by running

Table 7: Estimated contributions (in percent) to systematic errors on R .

Q^2 (GeV/c) ²	16.	18.
proton cross section	1.7	4.
G_E^n	0.89	0.39
Nuclear correction,	-	-
Accidentals	-	-
Target windows	.2	.2
Acceptance losses	0.16	0.11
Inelastic contamination	4.7	5.4
Nucleon mis-identification	0.5	0.5
HCal efficiency	0.5	0.5
Without proton err.		
Syst. error on G_M^n/G_M^p	2.38	2.73
With proton err.		
Syst. error on G_M^n	2.53	3.38

on a dummy target with thick aluminum windows. It should be possible to apply this correction with at least 5% accuracy (allowing for uncertainty in window thickness). So the systematic error on the correction should be under 0.17%.

11.1 Acceptance Losses

As discussed above, loss of nucleons from the acceptance of HCal can cause a systematic error, to the extent that the losses differ for neutrons and protons. A fiducial cut will be applied to select events which are similarly centered in HCal (as discussed in section 6) so the acceptance losses are kept small. The acceptance corrections are less than 2% in both cases. These losses result from the high momentum tail of the deuteron wave-function, which is identical for the neutron and proton. The cause of a difference in the corrections for the two nucleon species would be a difference in placement of the proton and neutron 'images' relative to the edges of HCal. It very conservative to allow for a possible 10% uncorrected difference in these corrections. This is entered as the systematic error contribution in Table 7.

This systematic error can be investigated (and perhaps even reduced) by examining the stability of the extracted ratio, R , as the fiducial cut is tightened or loosened from its normal value. Additionally, choosing a "window-frame" fiducial which preferentially selects events scattered near the edge of the HCal acceptance would allow investigation of the actual loss of protons and neutrons, which can be compared to Monte-Carlo estimates. Perhaps more importantly, such a study can be used to determine how closely the fractional losses of neutrons and protons are matched.

11.2 Inelastic Contamination

With the W^2 cuts described at the end of section 9 the predicted residual contamination of inelastic events in the quasi-elastic sample *before any corrections are made* are given in Table 3. These may be overestimated since the kinematics used for the inelastic simulation tend to exaggerate the effects of Fermi broadening. In the ratio R the contamination tends to cancel. More importantly, it should be possible to accurately estimate and subtract the inelastic contamination. The θ_{pq} distribution (shown in Fig. 17 and 18) beyond 1° gives a measure of the amount of inelastic contamination. The measured distribution can be extrapolated to small angle to estimate the residual contamination. It should certainly be possible to estimate the inelastic contamination at the 20% level. Assuming the numbers in Table 3 are reduced by such a factor, gives the contributions listed in Table 7. This is the largest contribution to the systematic error.

11.3 Nucleon mis-identification

Because of final state interactions or the long tail of the momentum distribution of the deuteron wave-function, some nucleons will be displaced far from the position predicted based on their \vec{q} vector and charge. This will result in mis-identification if a neutron is displaced sufficiently far upwards or a proton sufficiently far downwards. In the model used for the deuteron wave-function, about 5% of the nucleons have a component of momentum exceeding 100 MeV/c in any chosen direction. With a >370 MeV/c 'kick' being given to protons by the dipole, this should result in significantly less than 5% mis-identification rates. The cut on W^2 preferentially rejects events with large Fermi momentum, reducing the mis-identification rate still further. The misidentification of one species as the other and *vice versa* do not completely cancel because the proton rate is higher. However, the contamination will not go uncorrected. The neutron tail below the predicted point on the face of HCal can be measured without contamination from protons. Similarly the proton tail above the predicted point on HCal will be free of neutrons. Symmetry can then be used to predict the contamination of neutrons in the proton peak and, with minor kinematic corrections because of the deflection magnet, the proton contamination of the neutron peak. Since these tails originate from the same Fermi motion, the neutron and proton tails should be almost identical apart from minor distortion due to the deflection magnet. It should be possible to measure at the 10% level, the 'leakage' of neutrons/protons into the regions in which the other species is expected. A 10% error in the measurement of such a 1% tail would cause a systematic error of $\approx 0.2\%$ in the extracted value of R . In fact, stronger the field settings points should reduce the misidentification, so the error estimates in Table 7 are probably significantly overestimated.

11.4 Nucleon Detection Efficiency

For these highest- Q^2 points, no direct calibrations of neutron efficiency will be made. The proton and neutron efficiencies there are, however, both expected to be large and stable. The neutron efficiencies are expected to be over 95% so it seems inconceivable that they could be off by more than 5% (representing double the expected inefficiency). Furthermore, the proton efficiency must track closely with the neutron efficiency since both particles are detected by very similar hadronic showers. It seems certain that the efficiencies, which are expected to differ by only $\approx 1\%$, would have the expected ratio to within 0.1%. To be very conservative, we assign a systematic error 0.5%

in the efficiency correction, which is $\approx 50\%$ of the correction.

The final lines of Table 7 show the estimated total systematic error on G_M^n/G_M^p or on G_M^n found by adding the individual contributions in quadrature. In the former case the error on proton cross section does not contribute. Note that the fractional errors on these quantities are half of the quadrature sum of the errors on R simply because of error propagation thorough the square-root involved.

12 Installation

All the equipment used for this experiment is either already existing or planned for use in the Super-BigBite-Spectrometer (SBS) in Hall A.

- The BigBite spectrometer exists, but with different tracking instrumentation than is planned for this measurement.
- The GEM detector planes are planned as instrumentation of the polarimeter in the SBS
- The HCal calorimeter is planned as instrumentation of the SBS. Its design will be further optimized for Hall A applications, including the present experiment.
- The BigBen magnet is needed for an already-approved [63] 12 GeV experiment. Although we are using it only as a deflector magnet, it will eventually be the heart of the SBS.

All of this equipment is planned for use in essentially the same configuration in experiment E-09-019 (with the planned improvement in that experiment, using HCal in place of BigHAND). A major economization of installation time would be achieved by running the this experiment contiguously with E-09-019. Similarly commissioning time included in the E-09-019 run time would serve also for this experiment, greatly increasing the efficiency of beam usage. Beam time requested in this proposal is based on the assumption that the two experiments would run contiguously.

13 Beam Time Request

Given the simulation results for rate estimates and background contamination, an evaluation was made of the trade-off of statistical and systematic errors. Since the dominant systematic error is due to background contamination, that was the error considered in choosing a good trade-off of cuts which were tight enough to reduce systematic errors but not so tight as to require prohibitive running times. Table 8 gives the resulting contributions of statistical errors and background-related systematic errors to the determination of R for the requested beam times listed below, in Table 9.

Table 8 demonstrates that the beam hour requests have give a reasonable match of systematic and statistical errors. The statistics may be sufficient to allow data to be subdivided to study systematics. While higher statistics would be beneficial for that purpose, the requested beam time is sufficient so the statistical error does not dominate.

Because binomial statistics apply for the efficiency measurements, the number of required events is considerably smaller than might be expected for Poisson statistics. If N_{in} particles are incident

Table 8: Estimated statistical and systematic (from background subtraction only) errors on R for $W^2 - \theta_{pq}$ cuts optimized for the requested running times.

Q^2 (GeV/c) ²	16.	18.
Statistical (%)	2.5	4.1
Systematic (%)	4.7	5.4

on the detector, each with probability p of being observed, then the variance on the number of observed particles N_{obs} is

$$\sigma^2 = N_{in} p(1 - p) \approx N_{obs} (1 - p)$$

So the fractional error in the efficiency $\eta = N_{obs}/N_{in}$ is

$$\frac{\sigma_\eta}{\eta} = \frac{\sigma}{N_{obs}} = \frac{\sqrt{1 - p}}{\sqrt{N_{obs}}}$$

The required statistics for a given fractional error is therefore reduced by a factor of $(1 - p)$ compared to counting statistics. With expected efficiencies of over 0.95, this reduces the required number of calibration coincidences by a factor of 20.

Requested beam times are tabulated in Table 9. The first line lists the times, discussed above, found to give a suitable trade-off of statistical and systematic errors. Minimal time is also requested for calibration of the HCal detector with tagged protons and study of the alignment of HCal with BigBite. We also allow time for running at reduced luminosity to ensure that accidental rates are well understood. Elastic scattering measurements with the 48D48 deflector dipole turned off will be useful for checking the alignment of the \vec{q} inferred from BigBite measurements with the actual hit positions in HCal. Time is also allowed for running on dummy targets for subtraction of target window contributions. Eight hours are allowed to establish 11 GeV beam. Eight hours are allowed for each angle change. In total, 16 days are requested.

Figure 22 shows the size of the errors on the extracted values of G_M^n which would be obtained with the desired statistics and the systematic errors given in Table 7 (added in quadrature), see Table 10. The value is arbitrarily plotted at unity. The fractional error on G_M^n has been calculated using the projected error on the proton cross section. Because G_M^n is proportional to \sqrt{R} , the fractional error on R is scaled down by a factor of two to give the fractional error on G_M^n . The errors are seen to be far smaller than those on the existing data points above $Q^2 = 6$ (GeV/c)². Note that the projected errors on the measurements of E-09-019 are based on the experiment, as proposed. The actual errors may be smaller if the experiment is run with HCal, rather than BigHAND, for nucleon detection, as is now planned.

14 Relation to Other Experiments

This proposal does not overlap in measurements with any other approved or proposed experiment.

This experiment is closely aligned with E-09-019. The principle collaborators are the same, it is planned that the same equipment will be used, and the present experiment is intended to run contiguously with E-09-019.

Table 9: Beam Time Request (beam hours). “Normal \mathcal{L} ” refers to running at the standard luminosity of 2.8×10^{38} /A/cm²/sec. Reduced luminosity running is indicated as “Half \mathcal{L} ”.

Q^2 (GeV/c) ²	16.	18.	
E (GeV)	11.	11.	
θ_e	45.1°	65.2°	
θ_N	10.7°	7.0°	
d(e, e')			
Normal \mathcal{L}	96	192	
Dummy target	8	16	
H(e, e')			
Normal \mathcal{L}	6	12	
Half \mathcal{L}	2	6	
BigBen off	6	12	
Total	118	238	\Rightarrow 356
Commissioning			0
1 Energy change			8
2 angle changes			20
Beam request			384 (16 days)

Table 10: Estimated contributions (in percent) to errors on R, and resultant errors on G_M^n/G_M^p .

Q^2 (GeV/c) ²	16.	18.
proton cross-section	1.7	4.
G_E^n	0.89	0.39
Inelastic contamination	4.7	5.4
quadrature sum of other syst.	0.75	0.74
Statistical error	2.5	4.1
Without proton err.		
Total error on R	5.45	6.83
Error on G_M^n/G_M^p	2.72	3.42
With proton err.		
Error on G_M^n	2.85	3.96

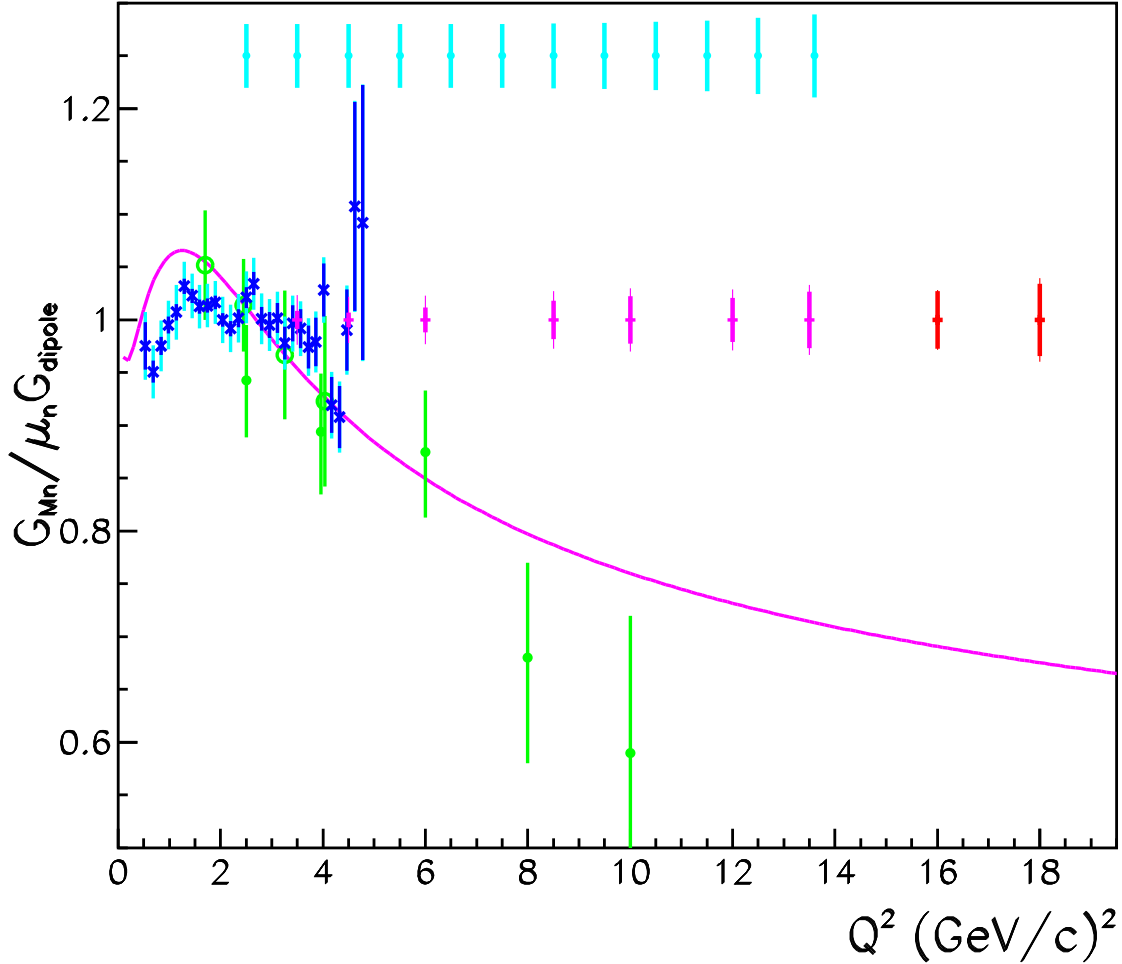


Figure 22: Existing data on G_M^n in the Q^2 range of the proposed measurement are plotted as ratio to scaled dipole approximation. (See caption of Fig. 1.) Magenta points (arbitrarily plotted at unity) show projected size of error bars for points approved for E-09-019. Red points show the projected errors for the measurements proposed here. Thick error bars include projected statistical and systematic errors of the proposed experiment but do not include errors on other measurements. Thin error bars include statistical and systematic errors and also estimated errors on G_E^n and on the proton elastic cross section. Solid light-blue circles with error bars (arbitrarily plotted at 1.25 for clarity) indicate the position and projected total errors [64] of the CLAS12 experiment.

This experiment would use similar equipment to the GEN experiment (E-02-013) [44] and many of the collaborators most involved in that experiment are also involved here. Technical expertise in tracking in BigBite and in calibration of a nucleon-detection arm will be available for this analysis.

The large dipole magnet, which is proposed for deflection of protons, is a part of an approved 12 GeV experiment which will measure Electric Form Factor of the proton at very large Q^2 [63].

High precision measurements of the neutron magnetic form factor were made at lower Q^2 in the CLAS e5 measurement (E-94-017). Many of the principle people involved in the analysis [40] of that data set are involved in the present proposal. This measurement will complement the CLAS measurement by extending the precision measurements to a far higher Q^2 . We will draw on much expertise and experience in controlling systematic errors in such a ratio measurement.

A 12 GeV experiment (E12-07-104) has been approved to extend the high-precision measurements of G_M^n out to $Q^2 \approx 13$ (GeV/c)² using the CLAS12 detector. Some of the spokespersons of that experiment are also involved in the present proposal.

The results from this experiment will be entirely complementary to those of E-09-019 and E12-07-104 in that the proposed experiment would extend the coverage $Q^2 = 18$ (GeV/c)².

CLAS12 is a large-acceptance device which, by its nature, collects data simultaneously at many scattering angles but with low luminosity. The proposed experiment collects data only at predetermined angles but can run at far higher luminosity (the planned luminosity for this proposal is over 2400 times the design luminosity for CLAS12). Systematic errors are more easily controlled for single-position detectors than for large acceptance detectors. The use of the same detector for both nucleon species also helps control the systematic errors in the proposed measurement. In the present proposal, the large baseline between the target and the hadron detector (17 m) also provides a major advantage in selection of quasi-elastic events due to superior angular and momentum resolution.

Since neutron-detection statistics dominate the statistical errors, Table 11 compares the expected statistics of Quasi-elastic neutrons detected in each experiments E-09-019, E12-07-104, and the present proposal. Because of the CLAS12 measurements are all made simultaneously, the statistics fall off rapidly at high Q^2 . In the present experiment and E-09-019 the high luminosity can be combined with beam times tailored to each kinematic point to make the statistics more even. It is seen that the present experiment not only extends the coverage to higher Q^2 than the CLAS12 experiment, but also beyond $Q^2 = 10$ (GeV/c)² the proposed measurements and E-09-019 have significantly higher statistics than the CLAS12 measurement.

15 Group Contributions to 12 GeV Upgrade

The following is a list of personnel from the institutions and their intended contribution to the proposed experiment:

- The CMU spokesperson and collaborators have long experience with neutron detectors and recent experience with the BigHAND detector (which includes 100 scintillator detectors provided by CMU). This group is participating in simulation of HCal and will lead efforts in design and testing of modules.
- The Hall A spokesperson and collaborators will be responsible for infrastructure of the 48D48 magnet, which is a part of three Form Factor experiments.

Table 11: Comparison of expected statistics of detected neutrons for CLAS12 experiment (E12-07-104), approved measurements (E-09-019) and present proposal. Note that statistics for E-09-019 are “as proposed” and will be even higher if HCal is used, as now planned. Dashes indicate points beyond the kinematic range of an experiment, asterisks indicate points for which no measurement is made. The last column lists the time allocated for data-taking in the present experiment. This may be compared to the total of 56 days (1344 hours) over which the CLAS12 experiment would acquire the statistics given in column 2.

Q^2 (GeV/c) ²	CLAS12 E12-07-104	Approved E-09-019	Present proposal	Hours
2.5	1.6×10^5	—	—	
3.5	2.3×10^6	2.1×10^5	*	12
4.5	6.6×10^5	1.4×10^5	*	12
5.5	89000	*	*	
6.0	*	28000	*	18
6.5	35000	*	*	
7.5	16000	*	*	
8.5	7700	11300	*	18
9.5	4000	*	*	
10	*	13900	*	24
10.5	2200	*	*	
11.5	1300	*	*	
12	*	4100	*	36
12.5	800	*	*	
13.5	500	2550	*	96
16	—	*	3660	96
18	—	*	1520	192

- The Rutgers spokesperson and collaborators will be responsible for preparation of the data acquisition components including front-end electronics and customized software.

In addition to equipment specific to this experiment, many collaborators are involved in projects in support of equipment for use in Hall A in the 12 GeV era. Many of these components are parts of the Super BigBite spectrometer (SBS) which will use the BigBen spectrometer and GEM detectors, among other components.

- The INFN collaborators are committed to provide a reconfigured tracker in BigBite and its operational support. They will also have a major role in implementation of the RICH in Hall A. The source of funding for this group is INFN. INFN has approved about \$150k for prototyping of the large GEM chambers and is supporting the whole front tracker in the GEP5 experiment including electronics for high resolution operation in SBS and BB.
- The UVA collaborators are responsible for construction and operation of high polarization high luminosity He target, which is a major part of the new GEN proposal to this PAC. The UVA collaborators are also responsible for reconfiguration of the tracker in the Super BigBite Spectrometer and its operation. The source of funding for this group is DOE. The University of Virginia group recently developed a major new tracker for the BigBite spectrometer.
- The Glasgow group intends to work on GEM-based detectors for the PANDA experiment and will share their results in hardware design and readout software with this effort, effectively contributing several FTE's.
- The Florida International University also intends to contribute in the development of a GEM-based tracker at least 1 FTE and put a graduate PhD thesis student in this experiment.
- The CMU group will use their expertise to implement the hadron calorimeter and the beam line magnetic shielding, both of which also required in the GEP5 experiment E12-07-109. This group has also become involved in the development of Compton polarimeter equipment for Hall A, and will continue that development into the 12 GeV era. The source of funding for this group is DOE.
- Along with the CMU group, College of William and Mary group, together with Dubna collaborators, intends to prepare the hadron calorimeter elements and their implementation in time for the experiment around 2014.

References

- [1] M.N. Rosenbluth, Phys. Rev. **79** 615 (1950).
- [2] M.K. Jones *et al.*, Phys. Rev. Lett. **84** 1398 (2000).
- [3] O. Gayou *et al.*, Phys. Rev. Lett. **88** 092301 (2002).
- [4] A.V. Afanasev *et al.*, Phys. Rev. D **72** 013008 (2005).
- [5] G. Miller, Phys. Rev. Lett. **99** 112001 (2007).
- [6] D. Kaplan and A. V. Manohar, Nucl. Phys. B **310**, 527 (1988).
- [7] R. D. McKeown, Phys. Lett. B **219**, 140 (1989).
- [8] D.H. Beck, Phys. Rev. D **39**, 3248 (1989).
- [9] D. Müller, D. Robaschik, B. Geyer, F.M. Dittes, J. Horejsi, Fortsch. Phys. 42 (1994) 101.
- [10] X. Ji, Phys. Rev. Lett. **78**, 610 (1997); Phys. Rev. D **55**, 7114 (1997).
- [11] A.V. Radyushkin, Phys. Lett. B **380**, 417 (1996); Phys. Lett. B **385**, 333 (1996); Phys. Rev. D **56**, 5524 (1997).
- [12] T. Eden *et al.*, Phys. Rev. C **50**, R1749 (1994).
- [13] M. Ostrick *et al.*, Phys. Rev. Lett. **83**, 276 (1999).
- [14] C. Herberg *et al.*, Eur. Phys. Jour. A **5**, 131 (1999).
- [15] Jefferson Lab experiment E-93-038, spokespersons: R. Madey, S. Kowalski.
- [16] I. Passchier *et al.*, Phys. Rev. Lett. **82**, 4988 (1999).
- [17] H. Zhu *et al.*, Phys. Rev. Lett. **87**, 081801, 2001.
- [18] M. Meyerhoff *et al.*, Phys. Lett. B **327**, 201 (1994).
- [19] H. Gao *et al.*, Phys. Rev. C **50**, R546 (1994); H. Gao, Nucl. Phys. A **631**, 170c (1998).
- [20] W. Xu *et al.*, Phys. Rev. Lett. **85**, 2900 (2000).
- [21] W. Xu *et al.*, Phys. Rev. C. **67**, R012201 (2003).
- [22] E.B. Hughes *et al.*, Phys. Rev. **139**, B458 (1965); *ibid.* **146**, 973 (1966).
- [23] B. Grossetête, S. Jullian, and P. Lehmann, Phys. Rev. **141**, 1435 (1966).
- [24] A.S. Esauslov *et al.*, Sov. J. Nucl. Phys. **45**, 258 (1987).
- [25] R.G. Arnold *et al.*, Phys. Rev. Lett. **61**, 806 (1988).

- [26] S. Rock *et al.*, Phys. Rev. D **46** 24 (1992).
- [27] A. Lung *et al.*, Phys. Rev. Lett. **70**, 718 (1993).
- [28] R.J. Budnitz *et al.*, Phys. Rev. **173**, 1357 (1968).
- [29] K.M. Hanson *et al.*, Phys. Rev. D **8**, 753 (1973).
- [30] P. Stein *et al.*, Phys. Rev. Lett. **16**, 592 (1966).
- [31] W. Bartel *et al.*, Phys. Lett. B **30**, 285 (1969); *ibid.* **39**, 407 (1972); Nucl. Phys. B **58**, 429 (1973).
- [32] P. Markowitz *et al.*, Phys. Rev. C **48**, R5 (1993).
- [33] H. Anklin *et al.*, Phys. Lett. B **336**, 313 (1994).
- [34] E.E.W. Bruins *et al.*, Phys. Rev. Lett. **75**, 21 (1995).
- [35] H. Anklin *et al.*, Phys. Lett. **B428**, 248 (1998).
- [36] G. Kubon *et al.*, Phys. Lett. **B524** 26 (2002).
- [37] J Lachniet *et al.*, Phys. Rev. Lett. **102**, 192001 (2009) JLab Experiment E-94-071
 “The Neutron Magnetic Form Factor from Precision Measurements of the Ratio of Quasielastic Electron-Neutron to Electron-Proton Scattering in Deuterium”, W. Brooks and M. Vineyard spokespersons.
- [38] A. Bodek *et al.*, Jour. of Phys. **110** 082004 (2008).
- [39] L. Durand, Phys. Rev. **115** 1020 (1959).
- [40] J. Lachniet thesis, Carnegie Mellon University, unpublished, June, 2005
http://www-meg.phys.cmu.edu/~bquinn/jeff_thesis.pdf
- [41] “Measurement of the Neutron Electromagnetic Form Factor Ratio G_{En}/G_{Mn} at High Q^2 ” proposal to PAC34, S. Riordan, G. Cates and B. Wojtsekhowski (spokespersons).
- [42] H. Arenhövel, private communication.
- [43] S. Jeschonnek and J.W. Van Orden, Phys. Rev. C, **62** 044613, 2000.
- [44] JLab experiment E-02-013, G.Cates, N.Liyanage and B.Wojtsekhowski (spokespersons).
- [45] S.Riordan, private communication.
- [46] See proposal of JLab Experiment E12-06-122 ”Measurement of neutron asymmetry A_1^n in the valence quark region using BigBite spectrometer.” G.Cates, N.Liyanage , Z.Meiziani, G.Rosner, X.Zheng and B.Wojtsekhowski (spokespersons).
- [47] N.V. Vlasov *et al.*, Inst. and Expt. Techniques **49** 41 (2006).

- [48] Pavel Degtiarenko, private communication.
- [49] Sergey Abrahamyan, private communication.
- [50] John Annand, private communication
- [51] Fatiha Benmokhtar, private communication
- [52] Rob Feuerbach, private communication.
- [53] J.L. Matthews and R.O. Owens, Nucl. Instr. and Meth. **111**, 157 (1973).
- [54] E12-07-104 proposal, “Measurement of the Neutron Magnetic Form Factor at High Q^2 Using the Ratio Method on Deuterium”, W. Brooks, G. Gilfoyle, K. Hafidi, and M. Vineyard spokespersons.
- [55] J.J. Kelly Phys. Rev. C **70**, (2004).
- [56] E.L. Lomon and H. Feshbach, Annals of Phys. **48** 94 (1968).
- [57] E12-07-108 proposal, “Precision Measurement of the Proton Elastic Cross Section at High Q^2 ”, J. Arrington, S. Gilad, B. Moffit, and B. Wojtsekhowski, spokespersons.
- [58] Data from PDG, <http://pdg.lbl.gov/xsect/contents.html> and references therein.
- [59] M.Ripani and E.M.Golovach based on P.Corvisiero, *et al.*, Nucl. Instr. and Meth. A, **3464** 33 (1994).
- [60] L.M. Stuart, *et. al.*, Phys. Rev. D **58** 032003 (1998).
- [61] L.Y. Zhu, *et. al.*, Phys. Rev. C **71** 044603 (2005).
- [62] R.L. Anderson, *et al*, Phys. Rev. D **14** 679 (1976).
- [63] JLab E12-07-109, Ch. Perdrisat *et al*, Large Acceptance Proton Form Factor Ratio Measurements at 12 and 15 $(\text{GeV}/c)^2$ Using Recoil Polarization Method.
- [64] G. Gilfoyle, private communication.